Spring 5-12-2017

BIOWASTE DERIVED RIGID POLYURETHANE FOAMS AND SUPERCAPACITORS: A RENEWABLE AND SUSTAINABLE ALTERNATIVE FOR PETROCHEMICALS

Charith K. R. Akurana Gamaralalage
cranaweera@gus.pittstate.edu

BIOWASTE DERIVED RIGID POLYURETHANE FOAMS AND SUPERCAPACITORS: A RENEWABLE AND SUSTAINABLE ALTERNATIVE FOR PETROCHEMICALS

A Thesis Submitted to the Graduate School
in Partial Fulfillment of the Requirements
for the Degree of Master of Science

Charith Kasun Ranaweera Akurana Gamaralalage

Pittsburg State University

Pittsburg, Kansas

April 2017

BIOWASTE DERIVED RIGID POLYURETHANE FOAMS AND SUPERCAPACITORS: A RENEWABLE AND SUSTAINABLE ALTERNATIVE FOR PETROCHEMICALS

Charith Kasun Ranaweera Akurana Gamaralalage

APPROVED:

Thesis Advisor _____
Dr. Ram Gupta, Department of Chemistry

Committee Member _____
Dr. Pawan Kahol, Department of Physics

Committee Member _____
Dr. Khamis Siam, Department of Chemistry

Committee Member _____
Dr. Charles Neef, Department of Chemistry

ACKNOWLEDGEMENTS

I wish to express my deepest gratitude to my advisor, Dr. Ram Gupta. His concepts and scientific knowledge helped me to initiate this research and directed me towards the achievement of the required objectives. His constant encouragement and guidance contributed immensely to conduct the research efficiently and effectively. I would like to convey my heartfelt thanks to Dr. Ram Gupta for his understanding at a personal level and enriching my research experience throughout the Master's program.

Furthermore, I am grateful to the Polymer Chemistry Initiative and Department of Chemistry at Pittsburg State University for offering me the opportunity to study in the Polymer Chemistry Program with a scholarship and providing funding for my research.

I want to extend my greatest appreciation to Kansas Polymer Research Center for making their facilities available to conduct experiments. Particular acknowledgement goes to Dr. Mihail Ionescu, Mr. Nikola Bilic, and Mrs. Xianmei Wan for their expertise and kind support, and Dr. Sanjay Mishra from University of Memphis for providing SEM images and Raman analysis of orange peel derived materials.

I wish to express my sincere thanks to Dr. Pawan Kahol, Dean of Graduate and Continuing Studies and Dr. Petar Dvornic, Chair of Department of Chemistry for their contribution of knowledge and for sharing their suggestions to improve the thesis work.

I wish to thank thesis committee, Dr. Pawan Kahol, Dr. Khamis Siam, and Dr. Charles Neef, for their service on the thesis committee and their valuable advice during the organization of my thesis.

Thanks to all my lab members and friends. It’s my pleasure to work with a very supportive group. Finally, I am deeply grateful to my family for their patient support, motivation, and encouragement throughout the Master’s program.

BIOWASTE DERIVED RIGID POLYURETHANE FOAMS AND SUPERCAPACITORS: A RENEWABLE AND SUSTAINABLE ALTERNATIVE FOR PETROCHEMICALS

An Abstract of the Thesis by
Charith Kasun Ranaweera

Bio-based polyol for rigid polyurethane (PU) foams and porous structured carbon as an electrode material for supercapacitors were synthesized from readily available biowaste precursor (orange peel) as an alternative to currently used petroleum-based starting materials. Synthesized bio-based polyols were characterized using FTIR, GPC, hydroxyl number, and viscosity measurements. These analyses indicated that intended bio-based polyol was obtained via thiol-ene chemistry with a high yield. Rigid PU foams prepared from bio-based polyol exhibited density around 35 kg/m^3, maintained a regular cell structure with uniform cell distribution, closed cell content over 90%, and excellent compressive strength of ~230 kPa, suggesting its suitability for thermal insulation applications. To improve the fire safety of rigid PU foams, dimethyl methyl phosphonate was added and fire resistance properties was regulated according to the horizontal burning test. Foams containing only 2 pbw of DMMP showed reduction in burning time by ~83% compared to the neat foam (without DMMP). TGA analysis indicated that the improved flame retardancy could be attributed to the release of DMMP at the temperature range of 100 °C to 250 °C.

Porous carbon prepared through KOH activation and pyrolysis demonstrated its potential as a high performing electrode material for energy storage. It was found that surface area and pore size of carbon can be controlled by varying the precursor to the KOH ratio. The specific surface area significantly increased with the increasing amount of KOH,

reaching specific surface area of 2,521 m^2/g for 1:3 mass ratio of precursor/KOH. However, the 1:1 mass ratio of precursor/KOH displayed the optimum charge storage capacitance of 407 F/g, owing to the ideal combination of micro-mesopores and higher degree of graphitization. The capacitive performance of the orange peel derived electrode was found to be varied with the electrolyte employed. The orange peel derived electrode in KOH electrolyte displayed the maximum capacitance and optimum rate capability. The orange peel derived electrode maintained above 100% capacitance retention during the 5,000-cyclic test and identical charge storage over different bending status. The fabricated supercapacitor device delivered high energy density (100.4 mWh/cm^2) and power density (6.87 W/cm^2), along with improved performance at elevated temperatures. This thesis demonstrates biowaste can be facilely converted into valuable starting materials for synthesis of polymers and energy storage devices.

TABLE OF CONTENTS

CHAPTER **PAGE**

LIST OF TABLES

TABLE **PAGE**

LIST OF FIGURES

FIGURE **PAGE**

CHAPTER I

1.0 INTRODUCTION AND LITERATURE REVIEW

Currently, crude oil and natural gases stand as the main source of energy in the world. However, we are even more dependent on petrochemical feedstock for raw materials and chemical building blocks to manufacture thousands of products, ranging from simple toys to pharmaceuticals. During the twentieth century, a remarkable growth of the chemical industry was observed with the wide availability and facile production process of petroleum [1]. Irreversible depletion of fossil fuel, volatile oil prices, adverse stresses on environment, and nonuniform distribution of fossil fuels have initiated the process of discovery for alternative sources. Bio feedstocks, such as agricultural products (not for food), agricultural waste, forestry feedstock, animal biomass, algae, and bacterial cellulose, offer renewable sources for primary chemicals and raw materials [2,3]. Although the utilizations of bio feedstocks are in early stages, the end of affordable fossil fuel is expected to significantly raise the demand for bio feedstocks around 2040 [4]. Already, the United States Department of Energy has planned strategies to obtain 10% of starting material from plant-based renewable resources by 2020 and plan to achieve a target of 50 % by 2050 [5].

1.1 Green Polyurethane

1.1.1 Present Status of Polyurethane

Polyurethane (PU) has rapidly progressed as a prominent polymeric material since its discovery as an excellent adhesive by Otto Bayer in 1937. Since its first discovery, polyurethane has been developed into versatile material, which can be used for various applications in modern life [6]. Polyurethanes are used in the form of rigid foams, flexible foams, thermoplastics, elastomers, coatings, and adhesives, for a wide range of applications such as building and construction, packaging, insulation, bedding and furniture, automotive, footwear, binding, and panting [7]. Polyurethane is the sixth mostly used polymer and it contributes to 5% of the total polymer market. Global PU production reached 18 million tons in 2016 and it is expected to grow by 7.4% during the period of 2016 to 2020 [8]. Among all forms of polyurethanes, rigid polyurethane foam (RPF) accounts for one-fourth of the PU market and it is the second most produced form of PU, after flexible polyurethane foam [9]. RPF is a combination of solid PU matrix and gases generated by a blowing agent, and approximately 96% of the total volume is occupied by the air. RPFs have emerged as a prime candidate for thermal insulation, sealant, and filling material due to their low thermal conductivity, low density, high compressive strength, dimensional stability, and low moisture permeability. In addition, use of RPFs can be found in refrigerators, boat flotation, buoys, and aircrafts [10].

Polyurethane foams are prepared via polyaddition reaction between diisocyanate and polyol (Figure 1.1) in presence of a blowing agent, catalyst, and surfactant. During foaming process, isocyanate also reacts with water (Figure 1.2), a commonly used blowing

agent to release carbon dioxide which responsible for the foaming process of the PU foams [11].

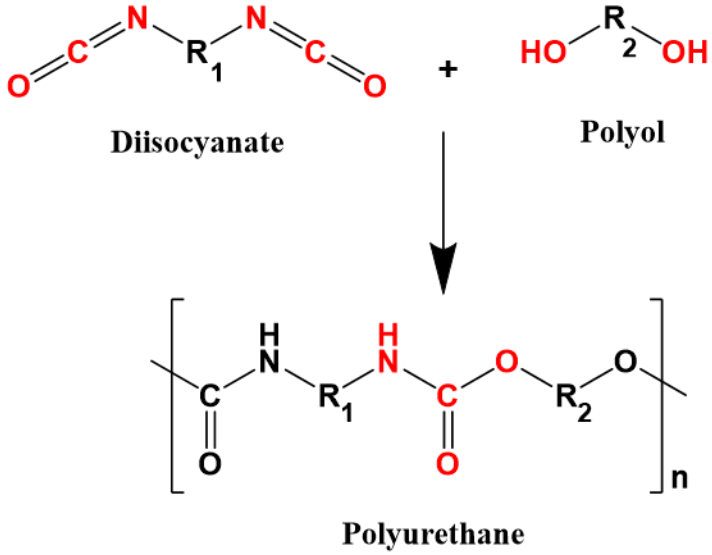

Figure 1.1 Reaction between diisocyanate and polyol to synthesis polyurethane

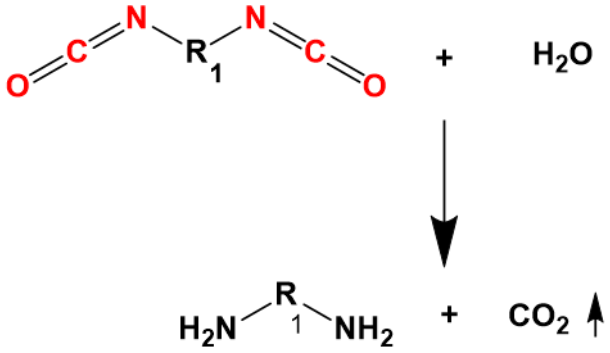

Figure 1.2 Reaction between isocyanate and water to release CO_2

Recently, the use of bio-based chemicals as the starting materials for polyurethane has gained considerable attention due to concerns over scarcity of petrochemicals, environmental issues, and competitiveness of bio-based PU to petrochemical counterparts. Extensive research has been focused on synthesizing plant derived isocyanates and polyols, two starting monomers of polyurethane, to replace the conventional petrochemical based

monomers. Generally, diisocyanates used for the synthesis of PU are derived from petrochemicals, and the use of bio-based diisocyanates are infrequently reported in literature. Isocyanate containing plant oil triglycerides were synthesized by brominating the triglyceride and subsequently reacting the brominated group with AgNCO to obtain isocyanate groups [12]. Synthesis of linear saturated diisocyanate was reported by Hojabri et al. using the Curtius rearrangement. This diisocyanate was derived from oleic acid and PU sheets prepared from plant-derived diisocyanate exhibited comparable physical properties to petroleum diisocyanate [13]. Various vegetable oils have been explored for the synthesis of polyol for polyurethane due to their low cost and wide availability. These vegetable oils consist of unsaturated triglyceride molecules which can be converted into hydroxy functional groups to obtain polyol for the subsequent reaction with diisocyanate. Soybean oil [14–16], castor oil [17,18], rapeseed oil [19,20], and palm oil [21,22] are the commonly used vegetable oils for the preparation of bio-based polyols.

1.1.2 Chemistry of Bio-based Polyols

So far, various plant derived oils have been explored for the synthesis of polyols for polyurethanes because of their sustainability, availability, and value for agricultural products, as well as their commercial competitiveness. However, most plant oils require additional reaction to incorporate hydroxyl functional group to undergo the reaction with isocyanate for the preparation of PU. Epoxidation [23–25], hydroformylation [26–28], ozonolysis [29,30], and transesterification [31,32] are among commonly utilized synthesis routes to modify the unsaturation of the triglycerides or fatty acids. These synthesis processes involve multi-step reactions or expensive catalysts, whereas thiol-ene chemistry offers a simple but efficient and rapid chemical route to functionalize the unsaturated

molecules. Thiol-ene chemistry proceeds through free-radical addition of thiols onto non activated double bonds under UV or heat initiation [33] as shown in Figure 1.3.

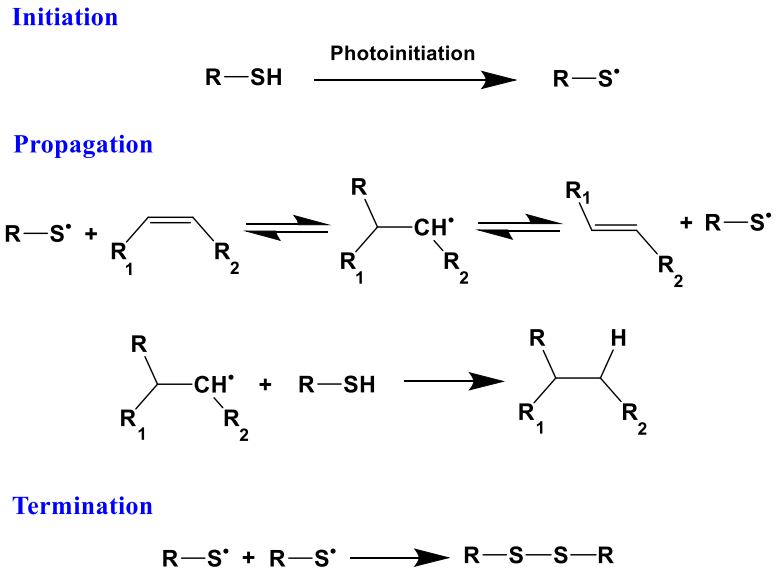

Figure 1.3 Mechanism of thiol-ene reaction

Thiol-ene coupling reaction has been used to alter the chemical structure of plant oils for various applications. Hydroxy thio-ether derivatives of vegetable oils were obtained by thiol-ene coupling to improve the wear and friction resistance of the vegetable oils [34–36]. Thiol-ene coupling is an effective reaction for crosslinking and oligomerization of vegetable oils with polyfunctional thiols under UV irradiation [37–39]. Notably, renewable monomers based on fatty acids have synthesized from thiol-ene reaction. Subsequently, monomers were polymerized to polyesters and polyanhydrides. These polymers exhibited fast degradation in hydrolytic condition, indicating their suitability for biomedical applications [40–42].

1.1.3 Flame-Retardant Polyurethane Foam

The main disadvantage of the polyurethanes is low flame retardancy due to the predominant presence of carbon, hydrogen, and oxygen in its structure. The highly porous and combustible nature of polyurethane foams further facilitate the flame spread rate [43]. Fire risks of polyurethane foams restricts some of its valuable applications [44]. Therefore, many studies have been conducted to improve the flame-retardant properties of polyurethanes. For example, phosphorous, nitrogen, aluminum, and expandable graphite containing compounds have been used as flame-retardant additives in polyurethanes [45–48]. Among them, phosphorous compounds were found to be effective additive flame-retardant.

1.2 Bio-based Electrode Materials for Supercapacitors

1.2.1 Supercapacitor as an Energy Storage System

Increasing demand for energy, deflation of fossil fuels, and environmental and economic concerns are driving the world towards production of sustainable energy, as well as development of efficient energy storage systems to harness the produced energy. Supercapacitors, or electrical double layer capacitors, are one of the advanced energy storage devices and have been drawing significant attention lately because of their unique advantages, such as pulse power supply, rapid charging time, outstanding service life, and operational safety [49,50]. As illustrated in the Ragone plot in Figure 1.4 [51], supercapacitors occupy a unique position among energy storage systems, since they deliver larger power density than all types of batteries and higher energy density than conventional capacitors. Due to these capabilities, supercapacitors are emerging as promising energy storage devices in 21st century over conventional energy storage devices for wide range of

applications in electrical vehicles, aircrafts, portable electronics, and energy harvesting systems [52,53].

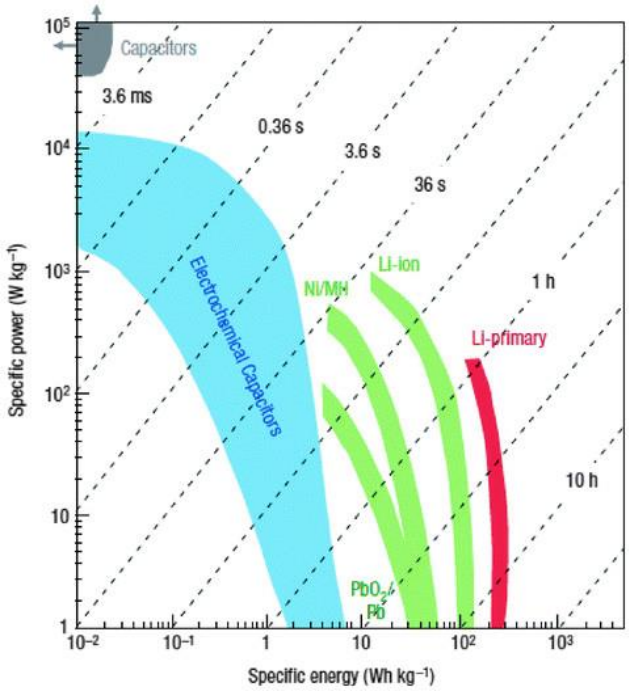

Figure 1.4 Ragone plot (specific energy vs specific power) for commonly used energy storage devices (adopted from ref. 51 with permission from Springer)

The typical structure of a supercapacitor includes two electrodes, separated by an ion transporting layer, immersed in an electrolyte solution. Energy stored in a supercapacitor is governed by two distinct electrochemical mechanisms, electric double layer capacitance (EDLC) and pseudocapacitance. In EDLC, accumulation of charges on the electrode/electrolyte interface leads to electrical energy storage, and pseudocapacitance is triggered by a reversible redox reaction, which results in electron transfer between electrode and electrolyte [54]. These two-electrochemical processes can operate simultaneously or individually, owing to the nature of the electrode material. Carbon based electrodes favor towards EDLC, while metal oxide, metal sulfide, and conducting polymers exhibit pseudocapacitance.

1.2.2 Biomass Derived Carbon for Electrode Materials

Thus far, various forms of carbon including activated carbon, graphene, carbon nanotubes (CNT), carbon nanofibers, and carbon aerogels have been exploited for supercapacitor applications due to their exceptional electrochemical and physical properties. Previously reported capacitive performance of these carbons are listed in Table 1.1 [55]. A tedious synthesis process and relatively high cost of advanced carbon allotropes such as CNT and graphene limit their extensive use in commercial energy storage devices. In contrast, activated carbon represents a cost effective yet facile synthesis process for carbon based electrode material compared to more advanced carbon allotropes.

Table 1.1 Specific capacitance of carbon-based materials in supercapacitors (adopted from ref. 55 with permission from Royal Society of Chemistry)

Carbon Material	**Specific capacitance in aqueous electrolyte**		**Specific capacitance in organic electrolyte**	
	F/g	**F/cm^2**	**F/g**	**F/cm^2**
Commercial activated carbons	<200	<80	<100	<50
Particulate carbon from SiC/TiC	170-220	<120	100-120	<70
Functionalized porous carbon	150-300	<180	100-150	<90
CNT	50-100	<60	<60	<30
Templated porous carbon	120-350	<200	60-140	<100
Activated carbon fibers	120-370	<150	80-200	<120
Carbon cloth	100-200	40-80	60-100	24-40
Carbon aerogels	100-125	<80	<80	<40

Commercial activated carbon is largely produced by carbonization of petroleum coke in an inert atmosphere [56], which is increasingly turning into expensive and environment damaging process. However, bio feedstocks offer a rich source of organic carbon, which can be easily converted into useful carbon material for supercapacitor electrodes. Lignocellulosic (cellulose, hemicellulose, and lignin) biopolymers are the primary constitution of plant biomass [57]. Among bio feedstocks, agricultural wastes attracted the most interest because of their low cost, wide availability, sustainability, and value addition. Sugarcane bagasse is a waste product generated from sugarcane milling. Porous carbon derived from sugarcane bagasse exhibited the specific capacitance between 142-300 F/g [58–60]. Rice husk is another agricultural waste which has extensively exploited for the supercapacitor electrodes. Rice husk based carbon exhibited a high specific surface area (2,804-3,145 m^2/g) and specific capacitance in the range of 147-367 F/g [61–63]. Biowaste such as corncob residue, coconut shell, sunflower seed shell, shaddock peel, oil palm kernel shell, waste coffee beans, waste tea leaves, and banana peel have been utilized as precursors to prepare activated carbon for electrodes in supercapacitors [64–71]. Bamboo is one of the widely-used plant materials for the preparation of activated carbons. Supercapacitors fabricated from bamboo based carbon demonstrated a specific capacitance between 258 to 510 F/g [72–74]. There are reports on use of plant material such as hemp, seaweeds, paulownia flower, dead leaves, cotton, and ramie fiber for supercapacitors [75–80].

Suitable pore structure and high surface area of electrode material and selection of appropriate electrolyte are key parameters that enhance the performance of carbon based supercapacitors [81]. In the last decade, several efforts have been focused on the continuous

improvement of biomass-derived activated carbon based electrodes. Preparation of activated carbons from biomass involves two processes, pyrolysis of precursor in an inert environment, accompanied with chemical or physical activation at higher temperature. Steam [82] and CO_2 [83] are the main class of physical activators. Chemical activation agents such as KOH [84], NaOH [85], H_3PO_4 [86], $ZnCl_2$ [87] have been employed to introduce porosity to carbon for numerous applications. Among them, KOH is the most attractive chemical reagent for the activation process of carbon used in supercapacitors because it produces high carbon yield, high porosity, and precise pore size distribution and ultrahigh surface area (~1 ml/g and ~3,000 m^2/g) [88,89]. Apart from the surface area and pore characteristics, the charge storage capacity of a supercapacitor depends on surface functionality. Incorporation of a surface functional group containing oxygen [90], nitrogen [91], or sulfur [92] can induce the pseudocapacitive behavior and increase wettability to improve the capacitance.

1.3 Orange Peel as a Starting Raw Material

According to the latest statistics from the United States Department of Agriculture, the estimated global orange production reached 49.6 million metric tons for 2016-2017 [93]. Among those, significant percentage of oranges are processed to manufacture fruit juice, 50–60% of which is discarded as waste [94,95]. A major portion of the waste consists of orange peel, and it accounts for about 44% of the total weight of the orange fruit [96]. As a widely available and readily collectable industrial biowaste, various applications including extraction of pectin [97], heavy metal adsorption [98], dye adsorption [99], production of biofuel [100], and starting material for polymers [101] have been proposed for orange peel to date.

Waste orange peel can provide renewable chemical building blocks to synthesize polyol for polyurethane. Citrus essential oil is the major component of the extract of orange peel, which consists of limonene as its major component (~96%) [102]. Citrus oil is extracted using simple techniques such as cold pressing, steam distillation, and solvent extraction [103]. Limonene is a hydrocarbon with a monoterpene structure (Figure 1.5). The monocyclic terpene structure of limonene presents several synthesis routes. For example, low molecular weight polylimonene and copolymer of limonene-maleic anhydride have been previously synthesized utilizing the Ziegler catalyst system and radical polymerization method, respectively [104,105]. The presence of internal and external alkene functional groups in the terpene structure opens the thiol-ene synthesis route for limonene with the thiol compound [106]. Janes et al. have synthesized thiols of limonene, α-pinene, α- and γ-terpenine, terpinolene, 3-carene and pulegone by reacting those with hydrogen sulfide using the thiol-ene reaction [107]. Marvel and Olson exploited the thiol-ene reaction to prepare dithiol from thioacetic acid and limonene, later polymerizing it with limonene to obtain a copolymer [108]. This thesis is focused on transforming limonene in to a polyol for subsequent synthesis of polyurethane foam with added benefit of safety from fire hazards.

Waste orange peel represents a great source of carbon. The composition of orange peel consists of approximately 71% carbon, 22% oxygen, 2% nitrogen, 2% hydrogen and 3% ash [109]. The presence of a larger carbon content suggests orange peel can be directly converted in to activated carbon for electrode material (Figure 1.5), ensuring a high value addition to the waste. For example, Arie et al. carbonized the orange peel in the presence of $ZnCl_2$ as the chemical activation agent and subsequently used it as electrode material in

a supercapacitor. Activated carbon exhibited a surface area of 1,200 m^2/g and an inferior capacitance of 56 F/g [110]. H_3PO_4 activated orange peel derived carbon has been used for electrodes in supercapacitors and as catalytic support for oxygen reduction reactions. Supercapacitor delivered a specific capacitance of 275 F/g [111]. These results indicate that there is still room for improvement. In this thesis, methods to control the architecture of orange peel derived carbon and the selection of electrolytes to maximize the charge storage capacity and electrochemical performance are presented, leading to an efficient use of biowastes.

Figure 1.5 Conversation of waste orange peel to useful stating materials

1.4 Motivation and Objective of the Thesis

Transition from today's petrochemical-dependent society toward a bio-biased society is becoming an essential requirement for maintaining a sustainable environment and economy. Therefore, substituting fossil fuel based material with renewable material has attracted great interest among the scientific world. However, the cost of producing bio-based materials remains expensive compared to fossil fuel based materials. The main aim of this thesis is to introduce a low cost and renewable biowaste (orange peel) for the synthesis of polyurethane and supercapacitor applications as a contribution to drive towards a greener world.

In the first phase, the primary objective was to prepare a flame-retardant and bio-based rigid polyurethane foam, starting from limonene (an extract from orange peel). Limonene polyol was synthesized via a thiol-ene reaction and characterized using analytical techniques and wet methods. Flame-retardant rigid polyurethane foams were synthesized starting from limonene polyol and by incorporating dimethyl methyl phosphonate (DMMP). Physical, mechanical, morphological, and fire resistance properties of RPF were characterized, in order to

- evaluate the viability of the thiol-ene reaction to synthesize bio-based polyol by reacting limonene and 1-thioglycerol;
- study the effects of bio-based polyol on the properties of RPF and compare them with commercial polyol based RPF; and
- investigate the effect of DMMP content on the properties of RPF.

The objective of the second phase was to engineer the orange peel derived carbon by employing a chemical activation agent for supercapacitor electrodes. A series of activated carbons, ranging from 0 to 3 mass ratios of chemical activation agent/OP were prepared, structurally characterized, and studied the electrochemical performance using three-electrode system and supercapacitor device in order to,

- control and obtain a suitable pore structure to maximize the charge storage capacitance;
- select an electrode-electrolyte system to deliver optimum power and energy density along with high rate capability; and
- design a porous carbon for long term stable, flexible, and high performance supercapacitor electrode.

CHAPTER II

2.0 BIO-BASED AND FLAME-RETARDANT RIGID POLYURETHANE FOAM

2.1 Experimental

2.1.1 Materials and Synthesis of Limonene Polyol

Limonene, 1-thioglycerol, and 2-hydroxy-2-methylpropiophenone were obtained from Sigma-Aldrich for the synthesis of limonene polyol (LTG). A commercially available polyol, soybean oil-based X-210 (OH content of 210 mg KOH/g), was received from Cargill and a sucrose-based polyether, Jeffol SG-520 (OH content of 520 mg KOH/g), was received from Huntsman. Rubinate M Isocyanate (polymeric methylenediphenyl diisocyanate, NCO content of 31%) was supplied by Huntsman. For the preparation of rigid polyurethane foams, catalysts DABCO T-12 and NIAX A-1 were purchased from Air Products and OSi Specialties, respectively. Silicone surfactant (Tegostab B-8404) was purchased from Evonik. Distilled water was the blowing agent. Dimethyl methyl phosphonate from Sigma-Aldrich was used as the additive flame retardant.

One-step thiol-ene chemistry was used for the synthesis of polyol based on limonene and 1-thioglycerol. In a typical synthesis, limonene (23.8 g) was added into 1-thioglycerol (37.8 g), which gave 1:2 molar ratio of limonene to 1-thioglycerol. The thiol-ene reaction was carried out at room temperature for 8 hours under 365 nm ultraviolet radiation in the presence of 2-hydroxy-2-methylpropiophenone (1.5 g) as the photo-

initiator. The reaction was carried out under constant stirring using magnetic stirrer at 300 rpm.

2.1.2 Preparation of Rigid Polyurethane Foams

Rigid polyurethane foams were prepared using limonene polyol, commercial polyols (X-210 & SG-520) and a blend of limonene polyol/commercial polyol (50/50 w/w ratio). Equivalent weight of isocyanate to polyol and distilled water was calculated based on the following equation:

$$w_i = Ew_i.\left(\frac{w_p}{Ew_p} + \frac{w_{pc}}{Ew_{pc}} + \frac{w_{water}}{Ew_{water}}\right) \quad \ldots (2.1)$$

where w_i, w_p, w_{pc} and w_{water} are the weights of isocyanate, limonene polyol, commercial polyol and water, respectively; E_{wi}, E_{wp} and E_{wpc} are the equivalent weights of isocyanate, limonene polyol and commercial polyol, respectively; and Ew_{water} = 9, which is the hydroxyl equivalent weight of water. RPFs were prepared according to the following procedure. Polyol, catalysts, surfactant, blowing agent, and fire retardant (DMMP) were mixed thoroughly to obtain a homogenized mixture using a high speed (6,000 rpm) mechanical stirrer. The effect of DMMP loading was studied by adding 0, 2, 4, or 6 parts by weight (pbw) to polyol. The detailed formulations are given in Table 2.1. After thorough mixing, isocyanate was added and the mixture was again stirred for several seconds. Finally, the mixture was allowed to rise at room temperature. Foams were kept at room temperature for 7 days to complete the curing process.

Table 2.1 Formulation of rigid polyurethane foams

Ingredient	0pbw-L/X	2pbw-L/X	4pbw-L/X	6pbw-L/X	0pbw-L/S	2pbw-L/S	4pbw-L/S	6pbw-L/S	2pbw-L	2pbw-X	2pbw-S
LTG	10	10	10	10	10	10	10	10	20	0	0
X-210	10	10	10	10	0	0	0	0	0	20	0
SG-520	0	0	0	0	10	10	10	10	0	0	20
NIAX A-1	0.2	0.2	0.2	0.2	0.2	0.2	0.2	0.2	0.2	0.2	0.2
Water	0.8	0.8	0.8	0.8	0.8	0.8	0.8	0.8	0.8	0.8	0.8
DABCO T-12	0.1	0.1	0.1	0.1	0.1	0.1	0.1	0.1	0.1	0.1	0.1
Tegostab B8404	0.4	0.4	0.4	0.4	0.4	0.4	0.4	0.4	0.4	0.4	0.4
Isocayanate	31.2	31.2	31.2	31.2	38.4	38.4	38.4	38.4	39.5	22.9	37.2
DMMP	0	2	4	6	0	2	4	6	2	2	2

* pbw- parts by weight

2.1.3 Characterization of Limonene Polyol

The synthesized polyol was characterized using various techniques. The phthalic anhydride/pyridine (PAP) method (ASTM-D 4274) was used to determine the hydroxyl number of the polyol. Gel permeation chromatography (GPC) was performed using a system by Waters (Milford, MA, USA). GPC was composed of four 300 × 7.8 mm phenogel 5 μ columns with different pore sizes of 50, 102, 103 and 104 Å. Eluent solvent

was tetrahydrofuran (THF) and eluent rate was 1 ml/min at 30 °C. The FTIR spectrum of the polyol was recorded using a Shimadzu IR Affinity-1 spectrophotometer at room temperature. Viscosity was measured by using an AR 2000 dynamic stress rheometer (TA Instruments, USA) at 25 °C with shear stress increasing from 1 to 2000 Pa linearly. The rheometer was equipped with a cone plate with an angle between 2° and a cone diameter of 25 mm.

2.1.4 Characterization of Rigid Polyurethane Foams

Physical properties, fire-retardant characteristics and morphology of RPFs were determined by the following standard procedures. The apparent density of foams was determined according to the standard test method for apparent density of rigid cellular plastics (ASTM D 1622). The closed-cell content of the foams was determined according to ASTM 2856 standard method by using Ultrapycnometer, Ultrafoam 1000. Cylindrical shape specimens of 45 mm × 30 mm (diameter × height) were used for both density and closed-cell content calculations. The compressive strength at 10% strain was measured according to the ASTM 1621 standard method by using a Q-Test 2-tensile machine (MTS, USA). The specimen sizes were 50 mm × 50 mm × 25 mm (length × width × height). Compressive force was applied parallel to the direction of the foam rise with a strain rate of 30 mm/min. The microstructure and morphology of the foams were observed using a Phenom G2 Pro scanning electron microscope (Netherlands). Before imaging, rectangular shape samples were cut with a sharp blade and attached with conductive carbon tape. Samples were gold sputtered to avoid the charging effect during imaging.

The thermal stability of RPFs was studied using thermogravimetric analysis (TGA) on a TA instrument (TGA Q500). Heating was carried out under nitrogen at a rate of 10

°C/min. Dynamic mechanical analysis (DMA) was performed on a TA instrument (TA 2980) which was operated on tension mode on a rectangular shape specimen (15 mm × 6 mm × 2 mm). Heating rate and mechanical vibration frequency were set as 3 °C/min and 10 Hz (amplitude: 15 µm), respectively. The fire-retardant properties of RPFs were studied according to the test method for horizontal burning characteristics of cellular polymeric materials (ASTM D 4986-98). Specimens of 150 mm × 50 mm × 12.5 mm were exposed to flame for 10 s. Burn time and weight difference (before and after the burning) were determined.

2.2 Results and Discussion

2.2.1 Synthesis and Characteristics of Limonene Polyol

The infrared spectra of the synthesized limonene polyol and its starting materials are shown in Figure 2.1. The appearance of a broad peak around 3,400 cm^{-1} in limonene polyol indicates the presence of alcohol (-OH stretching) group. This indicates the reaction between 1-thioglycerol and limonene. The peak around 2,550 cm^{-1} is the characteristic peak of S–H stretching of 1-thioglycerol. The disappearance of this peak in the FT-IR spectrum of the limonene polyol suggests that the reaction has been carried out. In addition, alkene group (C=C stretching) around 1,700 cm^{-1} in limonene has disappeared in the synthesized polyol. This further confirms the completion of the free radical initiated reaction between thiol and alkene groups of 1-thioglycerol and limonene, respectively, as shown in Figure 2.2. The thiol-ene reaction presented a single-step, cost-effective chemical route to hydroxy functionalize the limonene for the synthesis of polyols, compared to the tedious synthesis processes and expensive catalyst involved with the previously reported chemical route for the synthesis of polyols from plant materials [112].

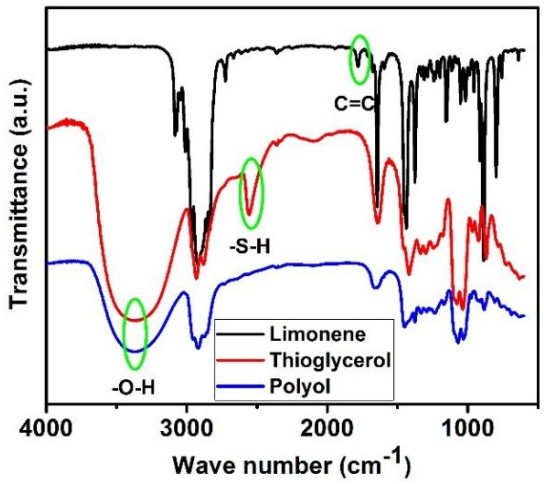

Figure 2.1 FTIR spectrums of limonene, 1-thioglycerol and limonene polyol

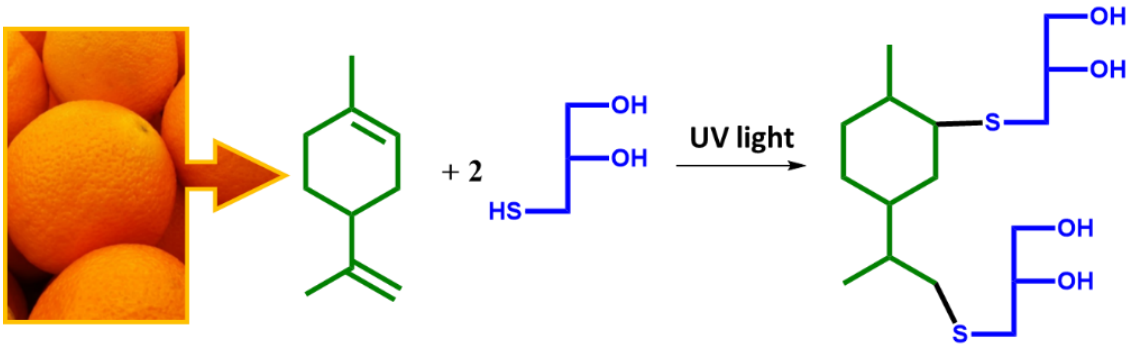

Figure 2.2 Synthesis of limonene polyol using thiol-ene chemistry

The hydroxyl number and viscosity of the limonene polyol were determined to be 569 mg KOH/g and 12 Pa.s, respectively. The GPC curves of limonene-based polyol and its starting materials (limonene and 1-thioglycerol) are shown in Figure 2.3. Overlay of the GPC curves further confirmed that majority of the limonene and 1-thioglycerol has been reacted to form limonene polyol. It can be seen in the GPC curve of the polyol that there was only a negligible amount of 1-thioglycerol residue. This suggests that the thiol-ene chemistry between limonene and 1-thioglycerol can be utilized successfully to synthesize the limonene polyol with a high yield. Two peaks in the GPC curve for the synthesized limonene polyol at 35.5 min and 36.9 min retention times were observed. These correspond to the two different types of molecular species in the synthesized polyol. The retention peak

at 35.5 min represents the higher molecular weight polyol species due to the addition of 1-thioglycerol to both the internal and terminal double bond of the limonene. The retention peak at 36.9 min might be the monoaddition of 1-thioglycerol to terminal double bond as a result of the reactivity difference in exocyclic and endocyclic unsaturation of the limonene [113].

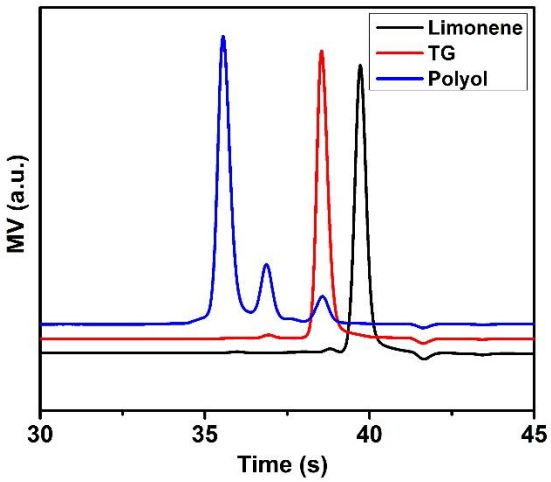

Figure 2.3 GPC spectra of limonene, 1-thioglycerol (TG) and limonene polyol

2.2.2 Properties of Rigid Polyurethane Foams

Figure 2.4a and b show the effect of DMMP concentration on the density of RPFs prepared using LTG-X 210 and LTG-SG 520 (50:50 w/w). It was observed that the density of the RPFs decreased with the increased in DMMP amount. For example, for RPFs prepared using LTG-X 210, the density decreased approximately by 10 kg/m^3 with increasing concentration of DMMP from 0 pbw to 6 pbw. Similar behavior was observed for the RPFs prepared using LTG-SG 520. Figure 2.4c compares the densities of RPFs containing 2 pbw of DMMP prepared using LTG (2pbwL), X 210 (2pbwX), SG 520 (2pbwS) and their 50/50 blends (2pbwL/X, 2pbwL/S). Densities of all foams were around

35 kg/m^3, which comply with the density required for the typical industrial applications (20–50 kg/m^3) [114].

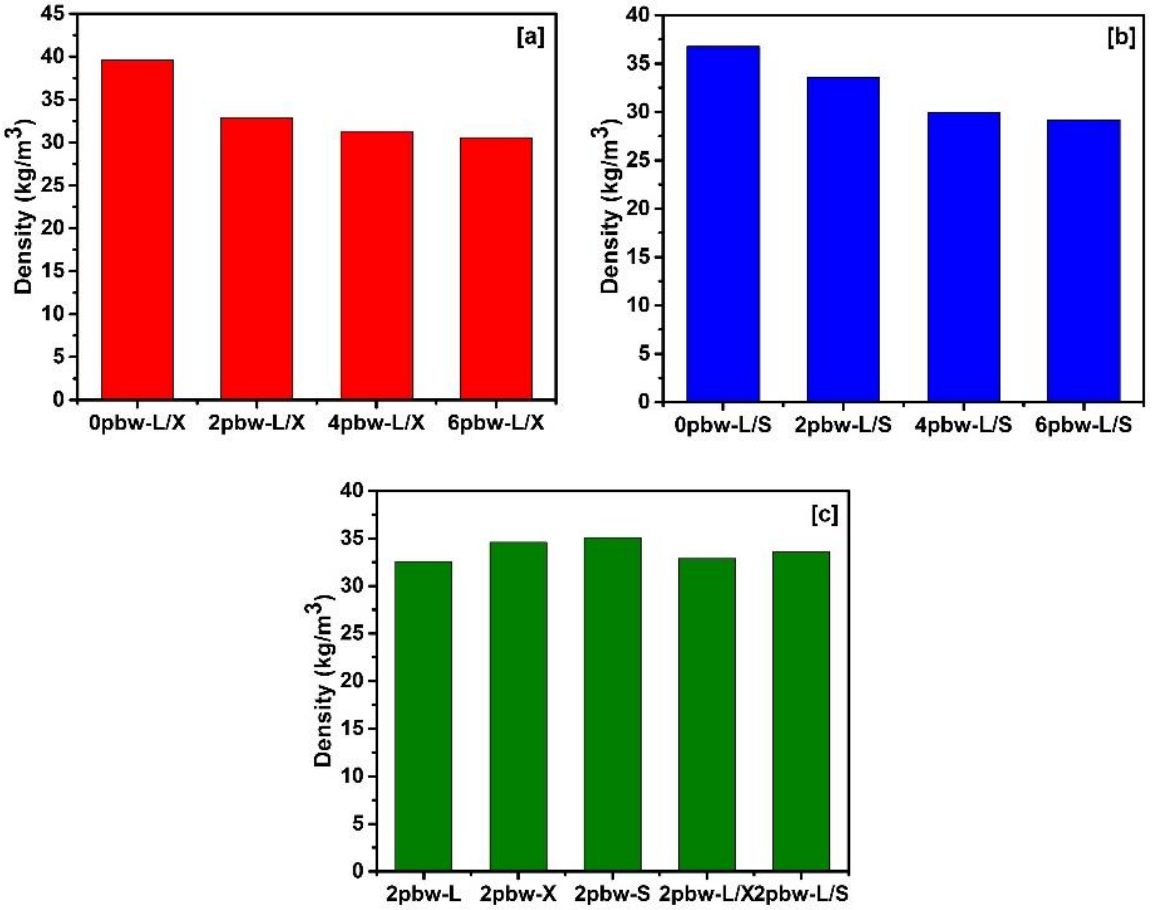

Figure 2.4 Density of the RPFs (a) LTG/X210, and (b) LTG/SG520 blends with different loadings of DMMP, and (c) limonene, X210, SG520 and their blends with 2 pbw of DMMP

Closed-cell content (CCC) is another important property of RPFs that should be considered. The CCC of all the polyurethane foams based on limonene and commercial polyol blends was above 90% even for the higher concentration DMMP (Figure 2.5a,b). This suggests that the RPFs prepared using limonene polyol blends may serve as a better thermal insulator due to the higher CCC percentage, which restricts the airflow through the foams. Figure 2.5c compares the CCC of RPFs containing 2 pbw of DMMP prepared using LTG (2pbwL), X 210 (2pbwX), SG 520 (2pbwS) and their 50/50 blends (2pbwL/X,

2pbwL/S). As observed, the CCC of all the foams was above 90%. The comparable CCC for the RPFs with and without DMMP suggests that addition of DMMP did not disturb the foaming process. The CCC of our prepared polyurethane foams was higher than those made using polyether polyol for flame-retardant polyurethanes [115].

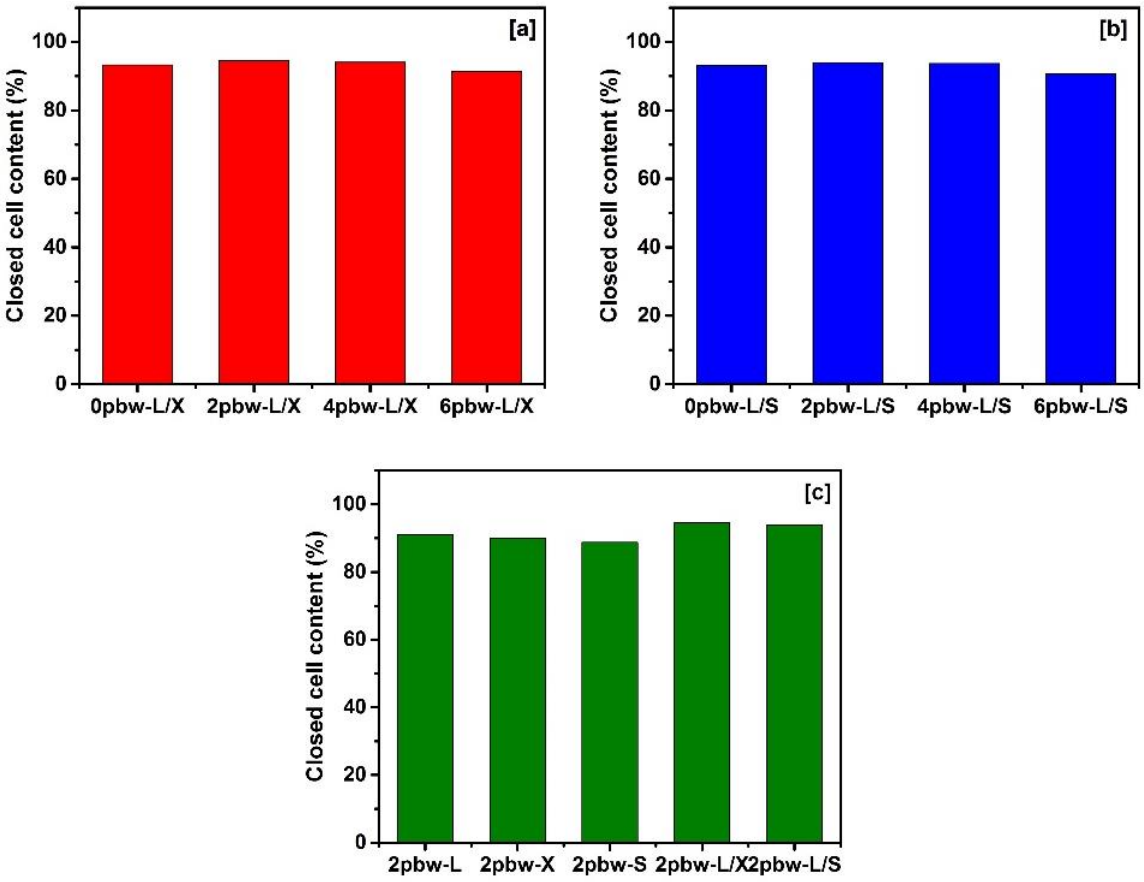

Figure 2.5 Close cell content of RPFs (a) LTG/X210 and (b) LTG/SG520 blends with different loadings of DMMP, and (c) limonene, X210, SG520 and their blends with 2 pbw of DMMP

The effect of the variation in density on compressive strength was eliminated by calculating the specific compressive strength (compressive strength/density) for all the foams, as presented in Figure 2.6. The compressive strength of the RPFs synthesized using limonene polyol was comparable to the compressive strength of polyurethanes prepared using commercial polyether-based polyol [116]. The highest compressive strengths of 233

and 226 kPa were observed for neat (without DMMP) polyurethane foams 0pbw-L/X and 0pbw-L/S, respectively. In contrast, the specific compressive strength of 0pbw-L/S was 4% higher than that of 0pbw-L/X. The higher specific compressive strength of the L/S blends was due to the superior hydroxyl numbers of the SG-520 polyol, which provided a maximum crosslinking density to the polyurethane network [117]. Specific compressive strength of RPFs seemed to not be affected by the addition of low concentration of DMMP. For example, the specific compressive strength of both 0pbw-L/X and 0pbw-L/S RPFs was reduced by approximately 5% when 2 pbw of DMMP was added. However, the continuous addition of DMMP from 2 pbw to 6 pbw significantly reduced the specific compressive strength (by nearly 30% in both types of RPFs). The decrease of the mechanical properties can be attributed to the release of lower molecular weight acidic substances due to the reaction between polyether polyol and DMMP. As a result, concentration of plasticizer increased and this influenced the change in properties [118]. It was further noted that RPFs based on limonene polyol have similar compressive strength to the commercial polyol-based RPFs (Figure 2.6c). However, when they were blended with a commercial polyol, the RPFs showed further enhancement in compressive strength.

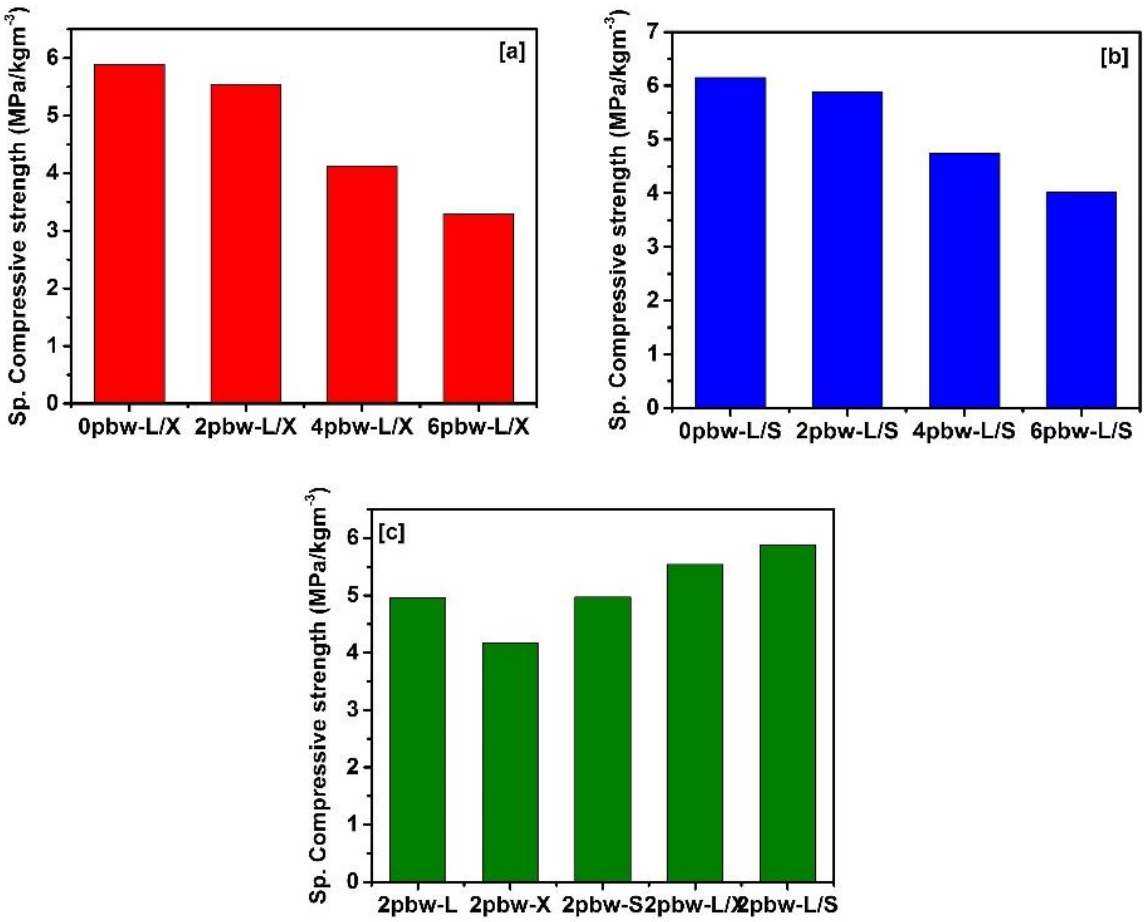

Figure 2.6 Specific compressive strength of RPFs (a) LTG/X210 and (b) LTG/SG520 blends with different loadings of DMMP, and (c) limonene, X210, SG520 and their blends with 2 pbw of DMMP

The microstructure and cell size distribution of the RPFs were studied using scanning electron microscopy (SEM). The SEM images of the polyurethane foams are shown in Figure 2.7. As seen in the SEM images, all the polyurethane foams had a polygon-shaped closed-cell structure which agrees with the above 90% closed-cell content measured from the gas pycnometer. Shape of the cell structure and cell size were uniformly distributed across the foams. Comparison of the SEM images of RPFs without DMMP (Figure 2.7a,e) and RPFs with DMMP (Figure 2.7b–d; 2.7f–h) revealed that average cell size increased with the incorporation of the fire retardant. For example, the average cell size of the polyurethane foams 0pbw-L/X, 2pbw-L/X, 4pbw-L/X and 6pbw-L/X was

observed as 100, 150, 150 and 175 μm, respectively. On the other hand, the foams 0pbw-L/S, 2pbw-L/S, 4pbw-L/S and 6pbw-L/S showed cell size of about 30, 150, 160 and 170 μm, respectively. This increase in cell size with the addition of the fire retardant might be attributed to the plasticizing effect of DMMP.

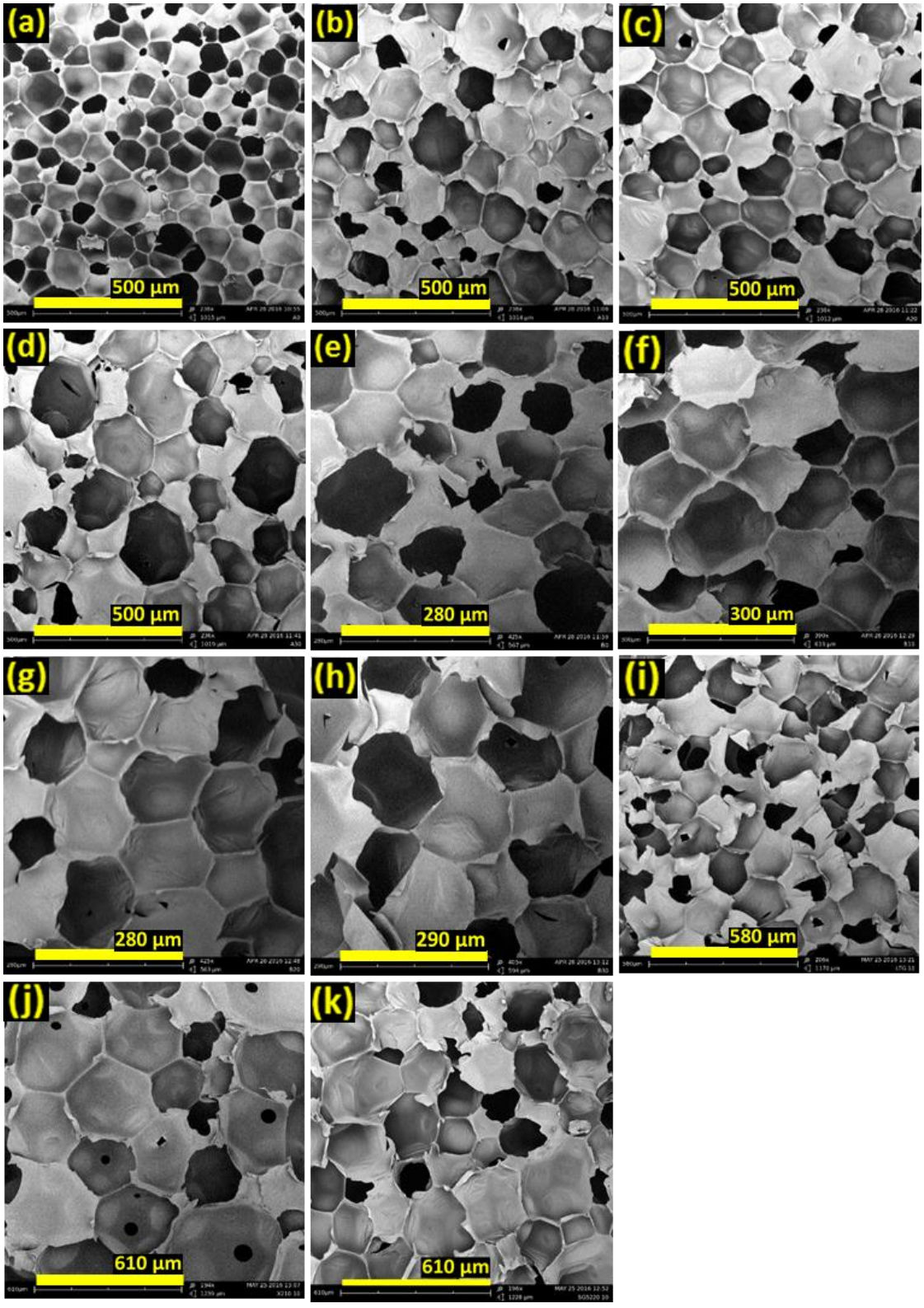

Figure 2.7 SEM images of RPFs (a) 0pbw-L/X, (b) 2pbw-L/X, (c) 4pbw-L/X, (d) 6pbw-L/X, (e) 0pbw-L/S, (f) 2pbw-L/S, (g) 4pbw-L/S, (h) 6pbw-L/S, (i) 2pbw-L, (j) 2pbw-X, and (k) 2pbw-S

Storage modulus and glass transition temperatures (T_g) of RPFs were determined using dynamical mechanical analysis (Figure 2.8). The maximum of tan delta was reported as the glass transition temperature of the RPFs. The glass transition temperatures of the L/X and L/S blends were around 228 °C and 242 °C, respectively. The T_g is affected by the crosslinking density. An increase in crosslinking density increases the T_g; therefore, higher T_g was observed for the L/S blends. Thermal stability of pure RPFs and DMMP containing RPFs were analyzed and illustrated in Figure 2.9. According to the TGA and DTGA curves, there were two and three thermal transitions in pure RPFs and DMMP containing RPFs, respectively. The first transition peak for all the DMMP containing samples appeared in the temperature range of 100 to 250 °C. On the other hand, pure RPFs without DMMP did not show any significant change in weight in a similar temperature range. This weight loss in flame retardant containing RPFs can be attributed to the volatilization of DMMP [119]. It was also observed that an increase of DMMP percentage increased the initial weight loss in fire retardant polyurethane foams. For example, an increase of the DMMP quantity in RPFs from 2 pbw to 6 pbw, increased the weight loss by 8% in both L/X and L/S samples. The main degradation phase in RPFs was observed between 250–400 °C. Significant weight loss (around 50% and 65% for sample L/X and L/S, respectively) in this temperature range might be due to the depolymerization of polyisocyanates and polyols after the cleavage of polyurethane main chain. As a result, some combustible gas products were generated [120].

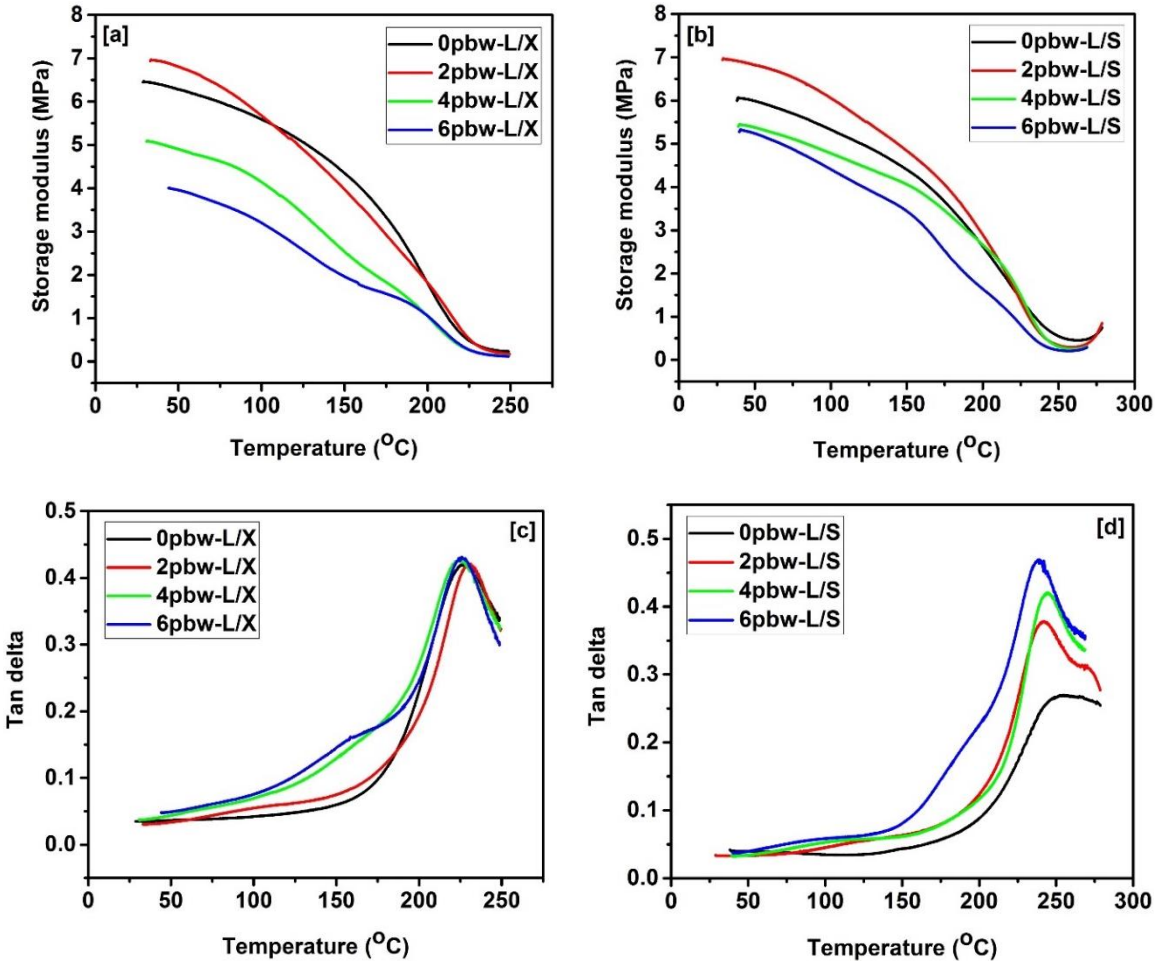

Figure 2.8 Variation of storage modulus in (a) LTG/X210 and (b) LTG/SG520 blends. Variation of tan delta in (c) LTG/X210 and, (d) LTG/SG520 blends

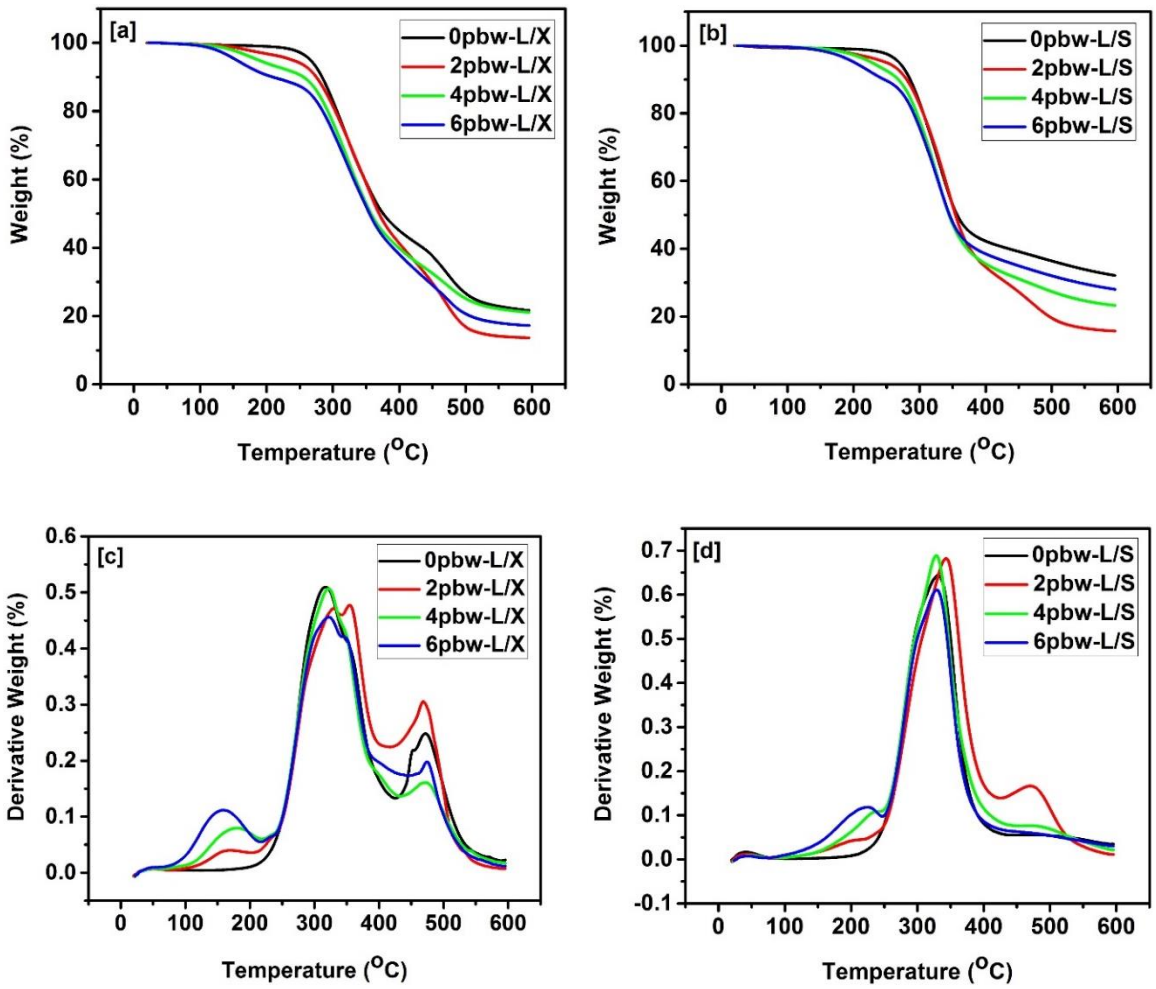

Figure 2.9 TGA curves of RPFs (a) LTG/X210 and (b) LTG/SG520 blends. DTGA curves of RPFs (c) LTG/X210 and, (d) LTG/SG520 blends

The initial thermal transitions of RPFs can be correlated to the burning test results in Figure 2.10a–c. Neat RPFs (without addition of DMMP) continued to burn for 110 s after the removal of the ignition source. However, RPFs with 2pbw of DMMP stopped burning after 19 s (Figure 2.10a,b). This enhanced flame-retardant property of DMMP can be explained as follows: under heating, DMMP released the phosphorous containing compound into the gaseous phase which was evident from the thermal transition peaks appeared between 100-200 ^{o}C in DTGA curves. These phosphorous compounds quenched the combustible products released during the decomposition of polyurethane foams [115].

In addition, the formation of a char layer also helped to prevent further burning. The flame-retardant mechanism of DMMP is further illustrated in Figure 2.11. An increase of DMMP quantity from 2 pbw to 6 pbw decreased the burning time by 5 s, which was due to the release of higher amounts of the phosphorus compound into the gaseous phase. Weight loss during the burning was also recorded and shown in Figure 10d–f. The RPFs without any flame retardant showed considerable loss of weight. However, the addition of even only 2 pbw of DMMP reduced the weight loss by almost 40%. This indicates that the DMMP acted as an effective flame retardant in limonene based polyurethane foam. Reference RPFs with 2 pbw of flame retardant showed comparable burning time and weight loss (Figure 2.10c, f), suggesting the suitability of DMMP as a flame retardant for different types of polyurethane compounds. The digital photographs of the polyurethane foams after the burring test are shown in Figure 2.12. As seen in the images, the addition of DMMP significantly reduced the burning of the polyurethane foams.

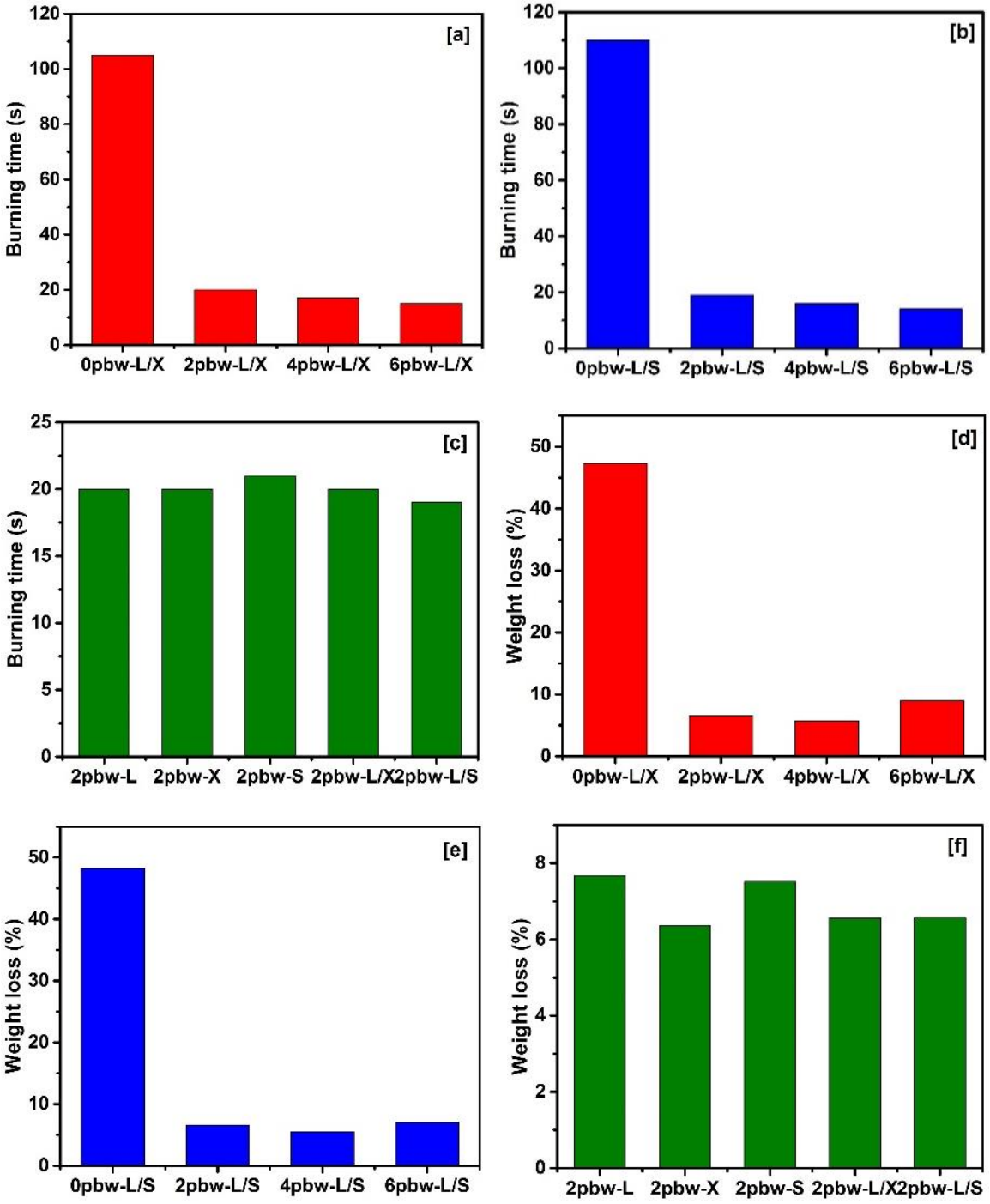

Figure 2.10 Burning time of RPFs (a) LTG/X210 and (b) LTG/SG520 blends with different loadings of DMMP, and (c) limonene, X210, SG520 and their blends with 2 pbw of DMMP. Weight loss during the burning test of RPFs (d) LTG/X210 and (e) LTG/SG520 blends with different loadings of DMMP, and (f) limonene, X210, SG520 and their blends with 2 pbw of DMMP

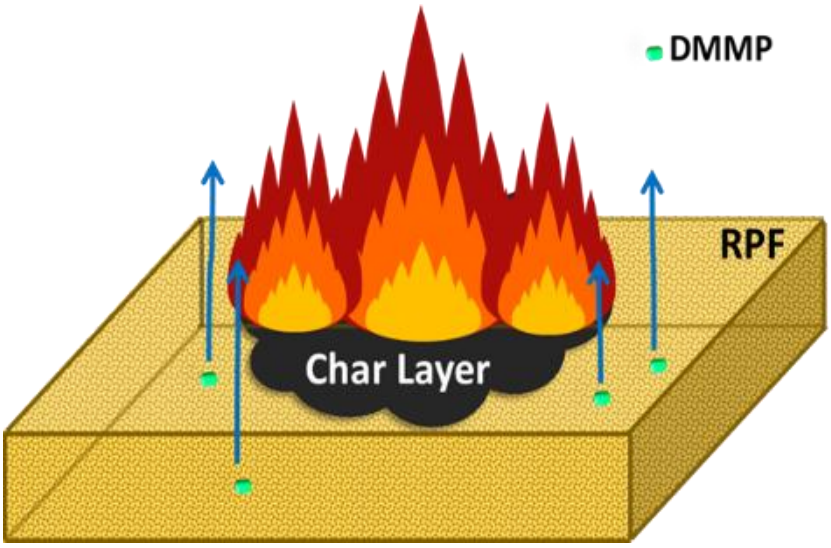

Figure 2.11 Flame retardant mechanism of DMMP in RPFs

Figure 2.12 Digital photographs of the foam after burring test

2.3 Summary

Limonene, an extract of orange peel, was reacted with 1-thioglecyrol using photochemically activated thiol-ene chemistry to successfully synthesize bio-based polyol. The bio-based polyol was suitable for preparation of rigid polyurethane foam with uniform cell morphology, high closed-cell content, and excellent mechanical properties. Incorporation of DMMP significantly enhanced the flame-retardant behavior of RPFs. The addition of 2 pbw DMMP to the pure RPF reduced the burning time from 110 s to 19 s. Further increments of DMMP concentration slightly improved the flame-retardant properties. However, addition of DMMP reduced the mechanical properties of the prepared foams. It was found that 2 pbw of DMMP was the optimum quantity of fire retardant, which exhibited balanced fire resistance and mechanical properties for the considered polyurethane foam matrix. Analysis of thermal stability and burning behavior of RPFs indicated that the decomposition products of DMMP may retard the combustion of polyurethane in the gaseous phase. Our study suggests that limonene polyol can be used for the preparation of rigid polyurethane foams. The addition of a small amount of DMMP in RPFs significantly reduced the fire hazard.

CHAPTER III

3.0 BIOWASTE DERIVED CARBON FOR SUPERCAPACITORS

3.1 Experimental

3.1.1 Materials and Synthesis of Activated Carbon

The waste orange peels were collected from household and subsequently washed, cleaned, and dried at 60 ^{o}C. Dried orange peels were crushed in to a fine powder. The obtained orange peel powder was pre-carbonized at 400 ^{o}C for 2 hours under nitrogen atmosphere. Subsequently, chemical activation of the resultant carbon powder was performed by using KOH as an activation agent. Carbon powder (1 g) and KOH pellets (1 g) were thoroughly mixed and pyrolyzed at 800 ^{o}C for 2 hours inside a tube furnace under a nitrogen flow. The collected black mass was ground into powder and rinsed with 1M HCl and DI water. The powder was dried at 60 ^{o}C overnight. The obtained sample was named OPAC-1. Accordingly, porous carbons with a different activation level were prepared by changing the mass ratio of KOH (1:0.5, 1:2, 1:3), these samples were named OPAC-0.5, OPAC-2, and OPAC-3. The sample without KOH activation (OPUAC) was used as the control.

3.1.2 Structural Characterization

To investigate the crystallite structure of synthesized carbon, X-ray powder diffraction (Shimadzu X-ray diffractometer) was conducted using 2θ-θ scan, employing

$CuK_{\alpha 1}$ (λ=1.5406 Å) as the radiation source. Raman spectroscopy (Model Innova 70, Coherent) was performed using an argon ion laser with a wavelength of 514.5 nm as the excitation source. Thermogravimetric analysis (TGA) was performed under nitrogen flow at a rate of 10 °C/min on a TA instrument (TA 2980). Morphology and microstructure of the carbon sample was determined by scanning electron microscopy (JEOL 7000 FE-SEM). Nitrogen adsorption/desorption isotherms were performed using an ASAP 2020 volumetric adsorption analyzer (Micrometrics, USA) at 77 K. Prior to the analysis, samples were degassed for 24 hours at 90 °C. The Brunauer-Emmett-Teller (BET) method and Barrett-Joyner-Halenda (BJH) theory were used to calculate the specific surface area and to derive pore size distributions, respectively.

3.1.2 Electrochemical Measurements

Electrochemical properties of the orange peel derived carbon (OPC) was evaluated utilizing three-electrode system and supercapacitor device. In both methods, electrodes were prepared by coating a viscous slurry of 80% (w/w) OPC, 10% (w/w) acetylene black, and 10% (w/w) polyvinylidene difluoride in N-methyl pyrrolidinone onto a nickel foam substrate. In the three-electrode system, electrochemical properties were studied using OPC coated nickel foam as a working electrode, a platinum strip as a counter electrode, and saturated calomel electrode as a reference electrode in three different electrolytes (3M KOH, NaOH and LiOH). A symmetrical supercapacitor was assembled by inserting an ion transporting layer between two identical OPAC-1 electrodes, followed by immersion in 3M KOH electrolyte. The cyclic voltammetry (CV), galvanostatic charge-discharge (GCD), and electrochemical impedance spectroscopy (EIS) were completed using a VersaSTAT 4–500 electrochemical workstation (Princeton Applied Research, USA).

Frequency range for EIS was varied from 0.05 to 10 kHz with 10 mV of AC voltage amplitude. The gravimetric capacitance (C_g / Fg^{-1}) for the three electrodes system and areal capacitance (C_a / Fcm^{-2}) for the supercapacitor were calculated from CV (Equation 3.1 and 3.2) and GCD (Equation 3.3 and 3.4) measurements:

$$C_g = \frac{Q}{\Delta V \times \left(\partial V / \partial t\right) \times m} \quad \ldots (3.1)$$

$$C_a = \frac{Q}{\Delta V \times \left(\partial V / \partial t\right) \times A} \quad \ldots (3.2)$$

Where, Q is the area under the CV curve (C), $\partial v/\partial t$ is the scan rate (V/s), ΔV is the potential window (V), and m is the mass (g) of the OPC, and A is the active area (cm^2) of the electrode.

$$C_g = \frac{I \times \Delta t}{\Delta V \times m} \quad \ldots (3.3)$$

$$C_a = \frac{I \times \Delta t}{\Delta V \times A} \quad \ldots (3.4)$$

where, I is the discharge current (A), Δt is the discharge time (s), ΔV is the potential window (V), m is the mass (g) of the OPC, and A is the active area (cm^2) of the electrode. The energy density (E / $Whcm^{-2}$) and power density (P / Wcm^{-2}) of symmetrical supercapacitor device was calculated according to the following equations:

$$E = \frac{C_a \times \Delta V^2}{7.2} \quad \ldots (3.5)$$

$$P = \frac{E \times 3600}{t} \quad \ldots (3.6)$$

where, C_a is the areal capacitance (Fcm^{-2}) calculated from galvanostatic charge-discharge measurements, ΔV is the potential window (V), and t is the discharge time (s).

3.2 Results and Discussion

3.2.1 Structural Properties of Activated Carbon

Figure 3.1 illustrates the conversion of waste orange peel to porous carbon through pre-carbonization and pyrolysis in the presence of a chemical activator. Subsequently, synthesized carbon was utilized to fabricate electrodes for symmetric supercapacitors.

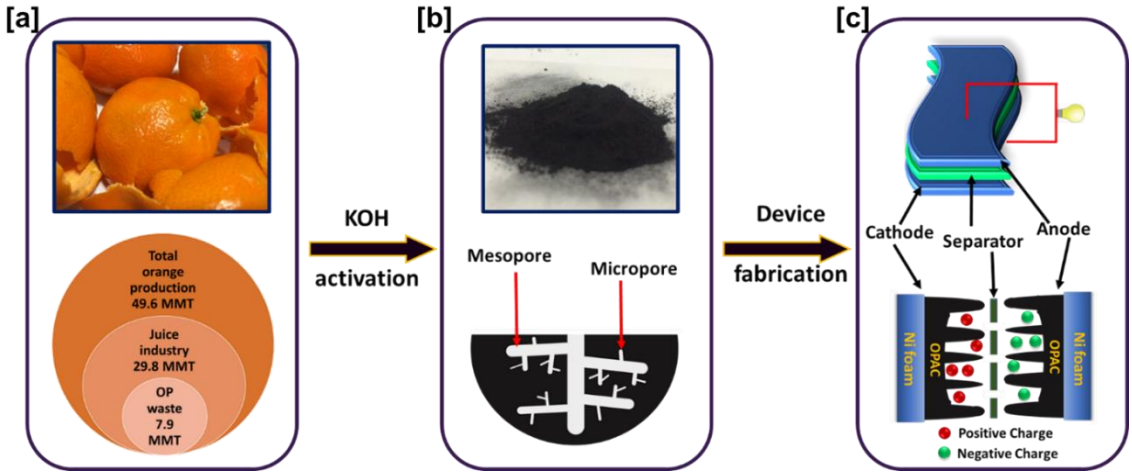

Figure 3.1 Schematic diagram for the preparation of supercapacitor from waste OP, (a) Image of raw OP and approximated calculation of OP waste generated in juice industry per year, (b) OP derived activated carbon and its pore structure, and (c) components of the fabricated supercapacitor

Figure 3.2a displays the XRD patterns of unactivated and activated carbonized OP with different mass ratios of KOH. XRD peaks center around 2θ of 24° and 44° in all the carbon samples and correspond to (002) and (100) planes of graphitic carbon. Broad and low intensity peaks indicate the disordered nature of the carbon samples. The characteristics peaks become broader and reduce intensity as the KOH mass ratio increases from 0 to 3, suggesting the decrease in graphitic structure in the OPACs [121]. These observations revealed that the degree of graphitization of the carbon sample was governed by the chemical activation agent. Further, the graphitic structure of unactivated and activated carbons were investigated by Raman spectra (Figure 3.2b). Two characteristics peaks around 1340 and 1582 cm^{-1} were assigned for D-band and G-band of carbon,

respectively. D-band corresponds to the sp^3 hybridized disordered carbon phase, while G-band relates to sp^2 hybridized graphitic phase of the carbon [122,123]. The proportion of the disordered carbon presence in a sample can be described by the relative intensity of D-band and G-band (I_D/I_G ratio). The I_D/I_G ratio for OPUAC was 0.88, whereas I_D/I_G ratios for OPAC-0.5, OPAC-1, OPAC-2, and OPAC-3 were found to be 0.91, 0.90, 0.91, and 0.96, respectively, considerably higher than the unactivated carbon sample. The rise of the I_D/I_G ratio for the KOH activated carbon suggests that harsh chemical treatment disturbed the structural order of the carbon. However, the graphitization level of our activated carbon materials ($I_G/I_D > 1.04$) are significantly higher than the I_G/I_D ratio of commercial activated carbon (0.52) [124], indicating its suitability as an electrode material due to excellent electrical conductivity. Pyrolysis behavior of orange peel precursor was analyzed under nitrogen atmosphere using thermogravimetric analysis. Thermogravimetric (TG) and its derivative (DTG) curves are given in Figure 3.2c. Generally, pyrolysis of biomass involves the thermal decomposition of lignocellulose material by releasing volatile matter and forming char. As seen in DTG curve, the appearance of peaks in the temperature range of 50-100 ^oC, 200-300 ^oC, and 300-400 ^oC can be attributed to the dehydration of orange peel and decomposition of hemicellulose and cellulose, respectively [125,126]. Lignin pyrolysis occurs steadily over a wide temperature range, the weaker peak between 430-500 ^oC may represent the decomposition of lignin. Lignin contributes predominately to the formation of char [127,128] and about 21% of char yield was observed at 700 ^oC.

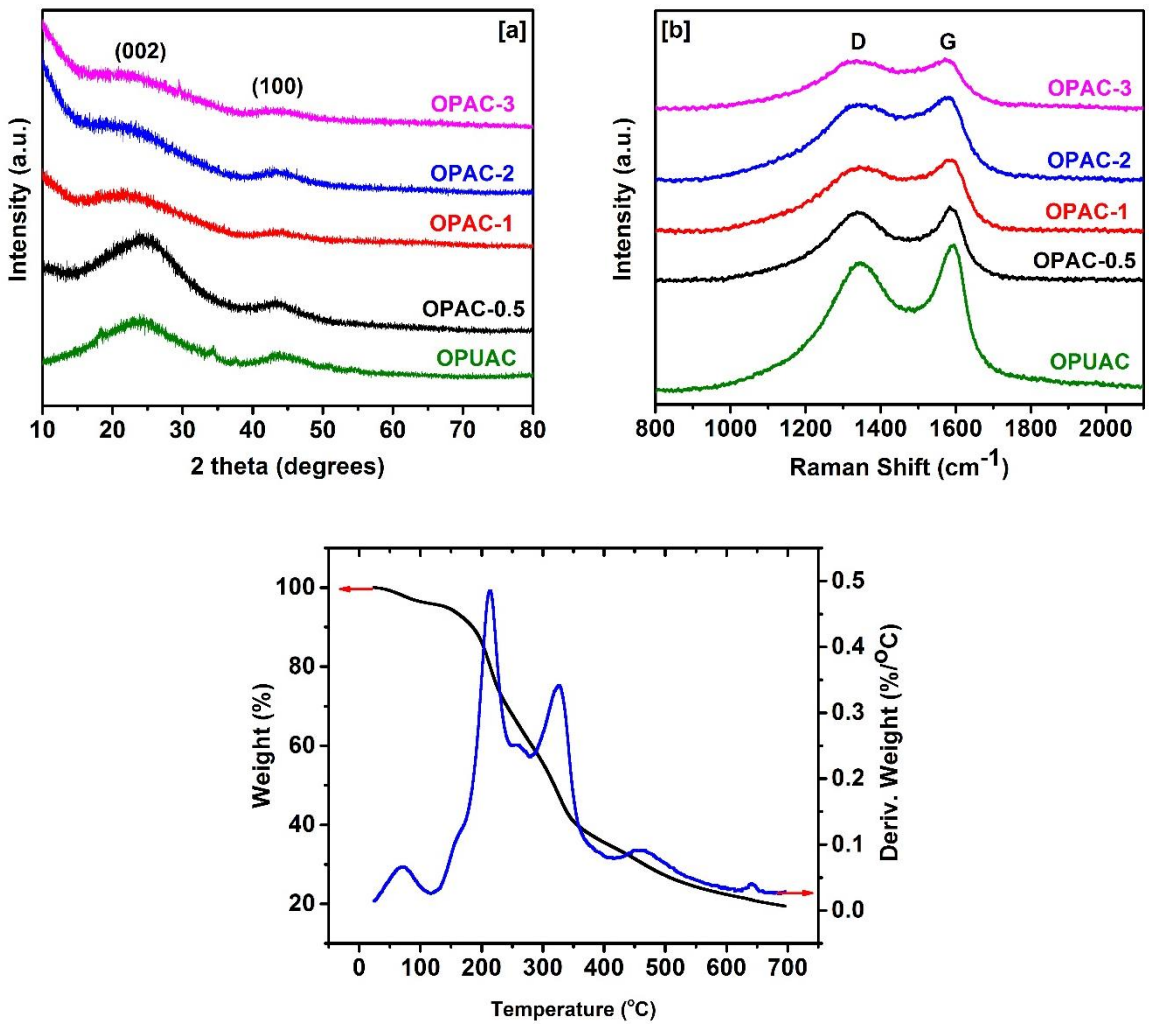

Figure 3.2 (a) XRD spectra and (b) Raman spectra of OPUAC and OPACs carbons, and (c)TG and DTG curves of orange peel powder

The SEM images in Figure 3.3 revealed the effect of chemical activation and pyrolysis on the morphology of carbon synthesized from the orange peel precursor. The pyrolysis of the pre-carbonized precursor in the presence of KOH (chemical activating agent) produced open channels with non-uniform honeycomb-like morphologies on the surface (Figure 3.3a-d). The pyrolysis of the pre-carbonized precursor without employing a chemical activating agent produced a sheet-like structure (Figure 3.3e). More prominent and widely spread honeycomb-like structures were observed with increasing KOH mass ratio. The schematic of the honeycomb and open tubular channels structures is illustrated

in Figure 3.3f. The presence of an open channel structure forms porous carbon, which provides electrolyte ions a higher surface area to access and a path for transportation during charge storage process [129,130]. The activation of the carbon by KOH at 800 ^{o}C proceeded according to the following reaction:

$$6KOH + C \rightarrow 2K + 3H_2 + 2K_2CO_3 \quad ...(3.7)$$

Subsequently, K_2CO_3 decomposed and the resultant products further reacted with the carbon to form the hollow chanels inside the carbon matix [131,132].

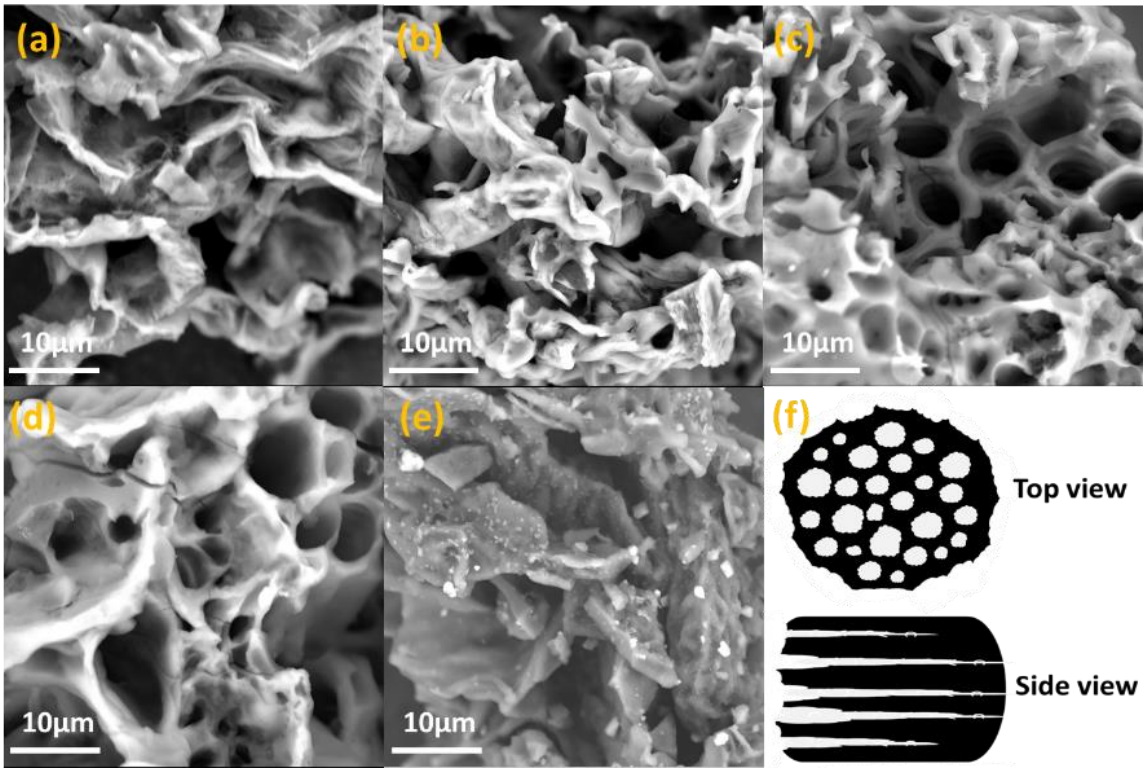

Figure 3.3 SEM image of (a) OPAC-0.5, (b) OPAC-1, (C) OPAC-2, (d) OPAC-3, (e) OPUAC, and (f) schematic diagram of porous structure in carbon derived from OP

The nitrogen adsorption-desorption isotherms of OPACs and OPUAC samples are illustrated in the Figure 3.4a. It was evident that pore structure and specific surface area of the resultant carbon were influenced by mass ratio of the activating agent. The OPAC-2 and OPAC-3 showed type I isotherm curves with the majority of N_2 adsorption at relative

pressures (P/P_0) below 0.3 and near parallel slope (to x-axis) of the isotherm above 0.3 of P/P_0, which is typical to micropores in the carbon. On the other hand, OPAC-0.5 and OPAC-1 showed combination of type I and IV isotherm curves with a sharp slope at relative pressure less than 0.1, followed by steady increase in the N_2 adsorption and the appearance of distinguishable hysteresis loops at P/P_0 over 0.5, demonstrating the existence of both micropores and mesopores [133]. In contrast, very low N_2 adsorption of OPUAC indicated the almost non-existent porous structure.

These observations were further confirmed by the BJH pore size distribution plot (Figure 3.4b). Pore size of OPAC-1 and OPAC-0.5 was mainly centered at the 3-4 nm range, along with a smaller fraction of pores around 2 nm, whereas OPAC-2 and OPAC-3 did not exhibit a complete distribution at smaller pore size end and overwhelmingly consisted of pores with a diameter of less than 2 nm. Therefore, the structure of OPAC-1 and OPAC-0.5 was a combination of meso-micropores with a larger proportion of mesopores. OPAC-2 and OPAC-3 contained abundant of micopores. Table 3.1 summarizes the pore characteristics of the carbon materials. Specific surface area of the OPAC-0.5 to OPAC-3 continuously increased from 1004 to 2521 m^2/g; similarly, pore volume also increased from 0.52 to 1.30 cm^3/g, respectively. Significantly lower specific surface area and pore volume were observed for OPUAC (0.852 m^2/g and 0.0004 cm^3/g, respectively). Nevertheless, pore diameter was reduced in the activated OP samples from 1.69 to 1.04 nm as the KOH mass ratio increased from 0.5 to 3. It was obvious that the progressive increment of the KOH mass ratio during the activation process continued to etch the carbon matrix deeper, while maximizing the pore volume and surface area instead of enlarging

pore diameter. Therefore, substantial proportion of micropores were created at higher KOH mass ratios.

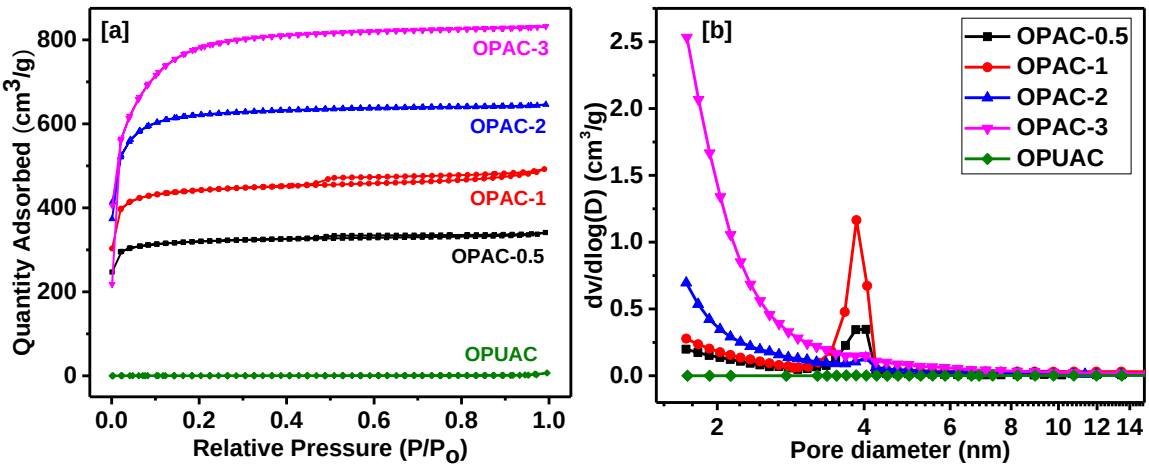

Figure 3.4 Nitrogen adsorption-desorption isotherms and (b) BJH pore size distributions of OPUAC and OPACs carbons

Table 3.1 Pore characteristics and surface area of unactivated and activated carbons

Sample	S_{BET}[a] (m^2/g)	V_{total}[b] (cm^3/g)	D_{ave}[c] (nm)
OPAC-0.5	1004	0.52	1.69
OPAC-1	1391	0.72	1.59
OPAC-2	1960	1.01	1.45
OPAC-3	2521	1.30	1.04
OPUAC	0.852	0.0004	1.16

[a] Surface area measured form BET method, [b] Total pore volume, and [c] Average pore diameter

The existence of both micro and mesopores is a favorable feature in activated carbon based electrode for supercapacitor applications. Presence of micropores provide larger surface for the adsorption–desorption process of electrolyte ions. Mesopores also ensure a highly accessible surface area and offer wider channels for several electrolyte ions

to diffuse at the same time without experiencing a geometric resistance [134,135]. Therefore, superior electrochemical performances in OPAC-1 were presumed due to the higher fraction of mesopores and enhanced surface area.

3.2.2 Electrochemical Properties of Activated Carbon

Electrochemical performance of supercapacitor electrodes based on OP derived carbon were studied employing three-electrode system in 3M KOH electrolyte. Figure 3.5a compares the cyclic voltammetry curves of OPUAC and OPACs at the scan rate of 10 mV/s. OPACs electrodes exhibited symmetrical rectangular shaped CV curves. In the absence of any redox peaks, this represents a typical electric double layer mechanism. In contrast, OPUAC had a smaller and highly distorted rectangular CV curve, indicating low charge storage capacity compared to OPUAC electrodes. Figure 3.5b displays the variation of specific capacitance at different scan rates for OPUAC and OPACs, suggesting that activated OP carbons have superior charge storage capacity than the unactivated OP carbon. Furthermore, OPAC-1 exhibited slightly higher specific capacitance compared to the other activated carbons. Galvanostatic charge-discharge profiles at current density of 1 A/g and specific capacitance at different current densities for the OPUAC and OPACs electrodes are shown in Figure 3.5c,d. The symmetric and linear nature of the charge-discharge profiles provided further evidence for the EDL behavior of the electrodes. Shortest discharging time and lowest capacitance of 115 F/g at 1 A/g was given by OPUAC. Chemical activation of the pre-carbonized OP significantly enhanced the capacitance. OPAC-1 provided the highest capacity of 217 F/g at 1 A/g and for the entire current density range (Figure 3.5d). OPAC-2 and OPAC-3 had higher specific surface area than that of OPAC-1, indicating that increased chemical activator amount and high surface

area did not always improve the charge storage capacity. Higher specific surface area of the OPAC-2 and OPAC-3 was attained through substantial presence of micropores. However, very narrow micropores restricted the ion transfer process, reducing the effective surface area for electrolyte ion adsorption. Therefore, OPAC-1 electrode provided the maximum capacitance.

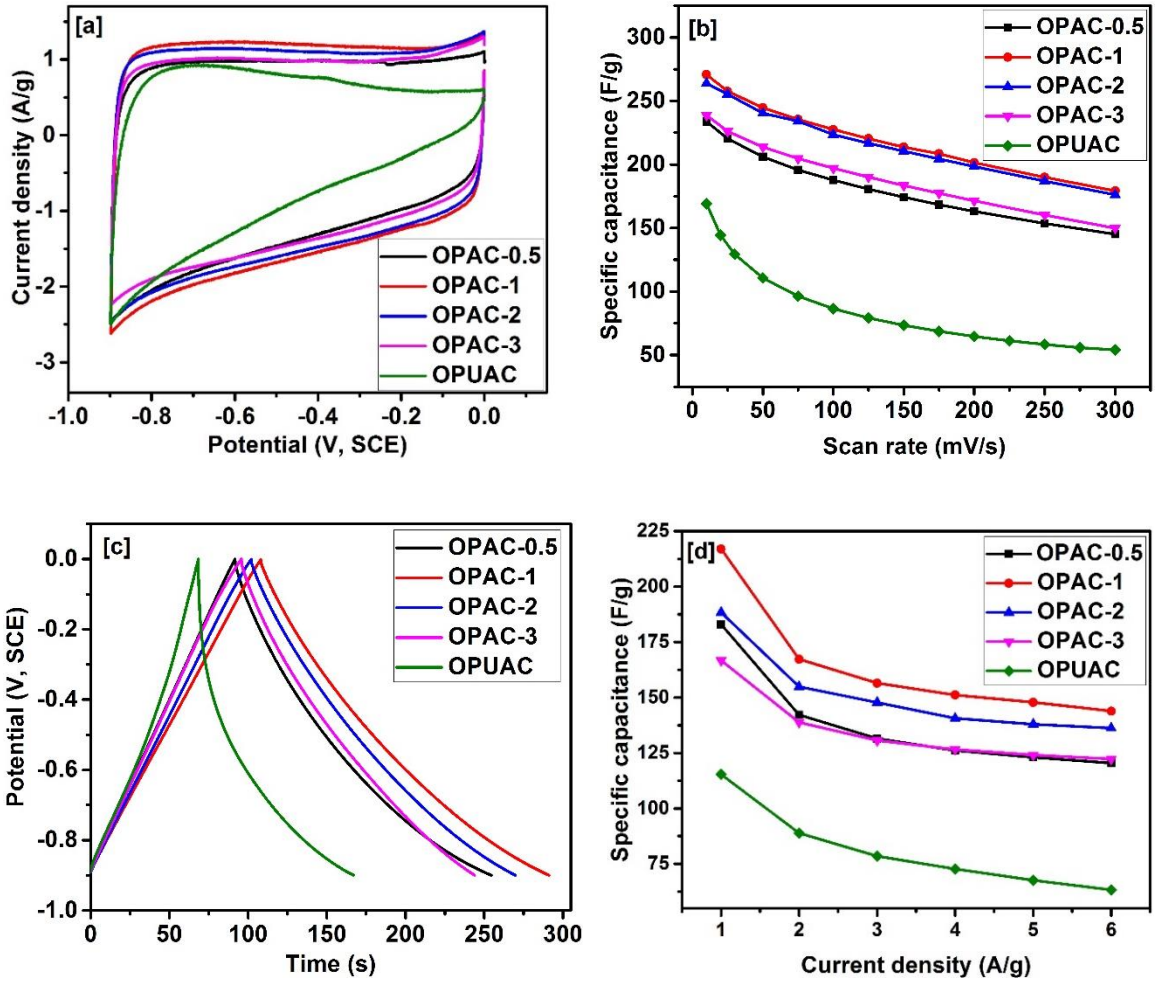

Figure 3.5 (a) CV curves at the scan rate of 10 mV/s, (b) Specific capacitances at various scan rates, (c) GCD profiles at the current density of 1 A /g, and (d) Specific capacitances at different current densities of OPUAC and OPACs electrodes in 3M KOH electrolyte

Electrochemical properties of OPAC-1 electrode were studied in detailed by performing CV at different scan rates (Figure 3.6a) and GCD at different current densities (Figure 3.6b). At low scan rates, CV curves exhibited a near perfect rectangular shape and

the shape was retained even at higher scan rates with a minor distortion, suggesting a rapid and unrestricted charge transfer process, owing to meso-/micropore combination of OPAC-1. As seen in the Figure 3.6b, charge-discharge profiles maintained linear and symmetric nature even at higher current densities, indicating an efficient electrolyte ion diffusion process. The IR drop (voltage drop) at the starting of the discharge curve accounts for total resistance in the electrode [68]. IR drop of 4 mV at 0.5 A/g was observed and it only increased to 194 mV even with a high discharge current of 20 A/g (Figure 3.6c,d).

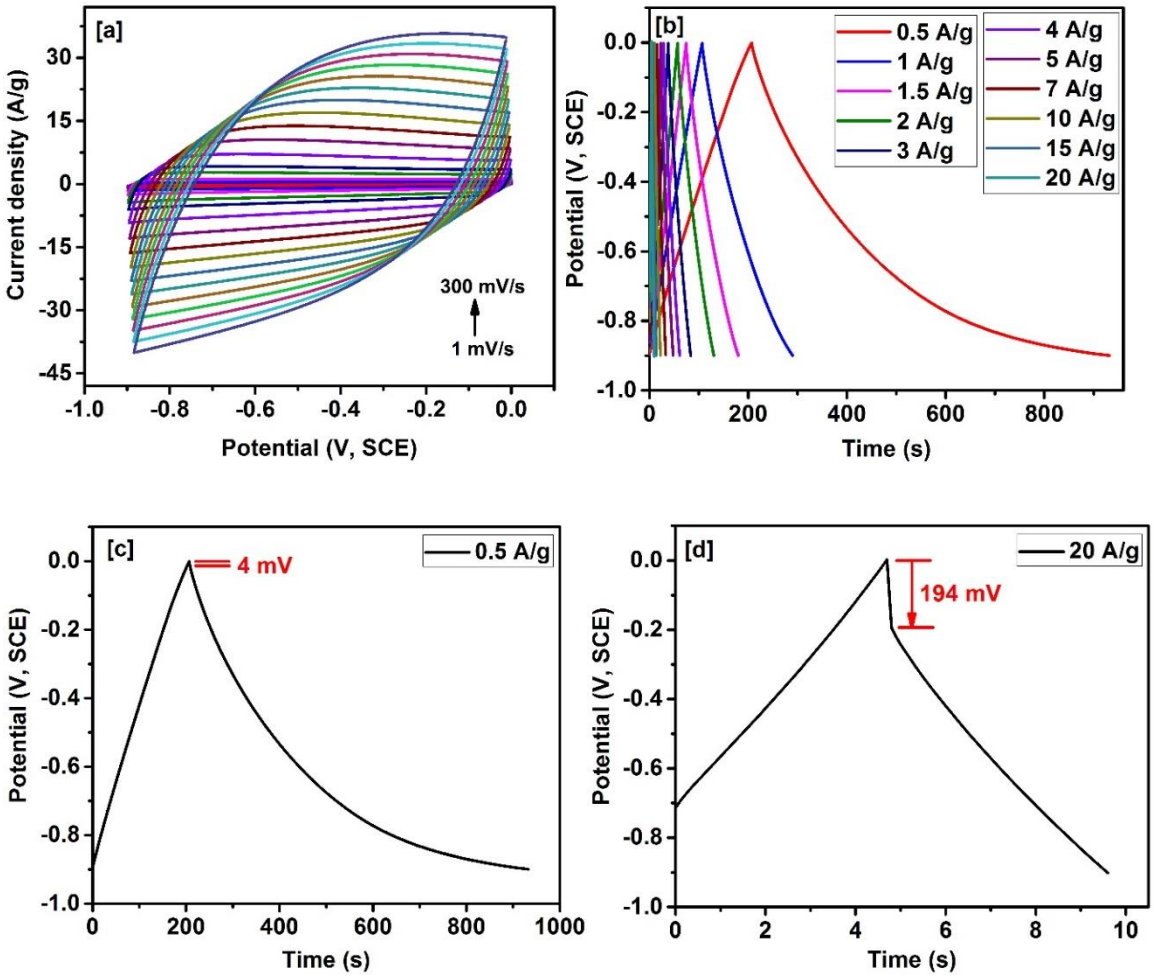

Figure 3.6 (a) CV curves at various scan rates, (b) GCD characteristics at different current, IR drop at current density of (c) 0.5 A/g and (d) 20 A/g of OPAC-1 electrode in 3M KOH electrolyte

Figure 3.7a illustrates the CV curves for different bending angles at a scan rate of 100 mV/s. Shape of the CV curves remained identical, indicating that OPAC-1 electrode sustained its electrochemical properties under flexing. This suggested potential application of OPAC-1 electrode in flexible supercapacitors. Long term cyclic stability of a supercapacitor is another important feature that determines its practical applicability. Cyclic stability of OPAC-1 was evaluated by performing continuous charge-discharge cycles at 3A/g (Figure 3.7b). The capacitance for first 500 cycles gradually increased until capacitance retention reached to 105%, followed by an almost steady capacitance delivery. The capacitive performance improved to 108% of its initial value over 5,000 cycles. The initial improvement in capacitance was due to the activation of the OPAC-1 electrode by progressive wetting of the electrode with electrolyte [136,137]. Perfectly overlapped charge-discharge profiles of first and last five cycles (inset in Figure 3.7b) provided further evidence for the excellent long term cyclic stability of OPAC-1.

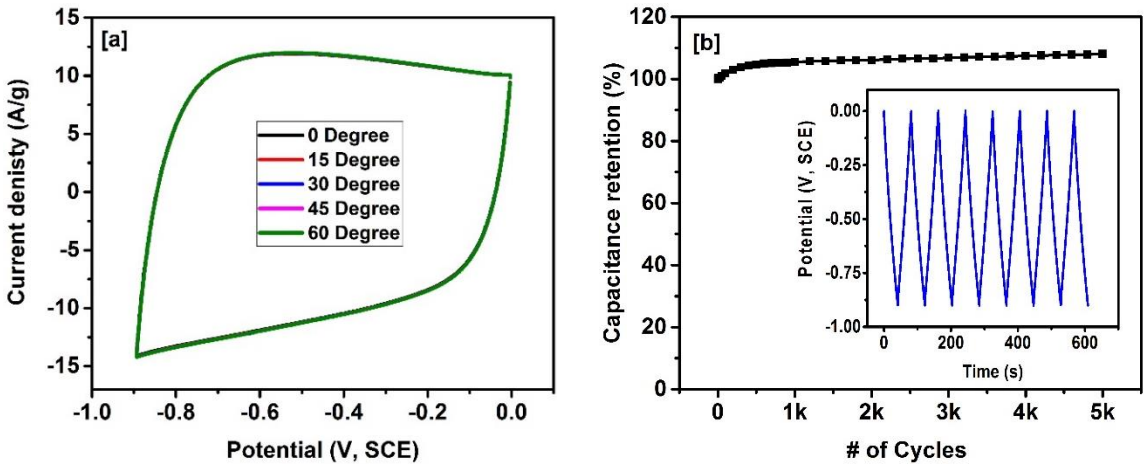

Figure 3.7 (a) CV curves for various bending angles at the scan rate of 100 mV/s and, (b) Cyclic stability at current density of 2 A/g for 5,000 cycles and inset shows GCD profiles of first and last few cycles of OPAC-1 electrode in 3M KOH electrolyte

To understand the effect of electrolytes, the specific capacitance of OPAC-1 was measured in 3M KOH, 3M NaOH and 3M LiOH at different current densities (Figure 3.8a)

and scan rates (Figure 3.8b). OPAC-1 exhibited highest specific capacitance of 407 F/g at a current density of 0.5 A/g and 320 F/g at a scan rate of 2mV/s in KOH electrolyte. Also, OPAC-1 delivered superior capacity than NaOH and LiOH electrolytes across the measured current density and scan rate range. The improved electrochemical properties in KOH electrolyte can be ascribed to smaller hydrated ionic radius of K^+ (3.31 Å), which is lower than the hydrated ionic radius of the Na^+ (3.58 Å) and Li^+ (3.82 Å). The ionic conductivity of hydrated ions increases with a decrease in ion size [134]. This facilitated the access to innermost pores of the OPAC-1 for the K^+ and reduced the transition time between the adsorption-desorption process. Therefore, OPAC-1 in KOH electrolyte exhibited the maximum charge storage capacity. Also, a different rate behavior of OPAC-1 was observed in these electrolytes. Figure 3.8c,d displays the CV curves of OPAC-1 at 10 and 200 mV/s in KOH, NaOH and LiOH. The area under the curves were almost equal at low scan rate, indicating similar charge storage behavior in three electrolytes. In contrast, charge storage capacity deviated at a high scan rate, increasing order of LiOH < NaOH < KOH. The least decayed of capacitance in KOH electrolyte can be credited to the smallest hydrated radius of K^+ among three metallic ions. Therefore, hydrated K^+ possessed the highest ionic conductivity and shortest relaxation time during the diffusion process, resulting an increment in the rate capability of OPAC-1 in LiOH < NaOH < KOH, in this order.

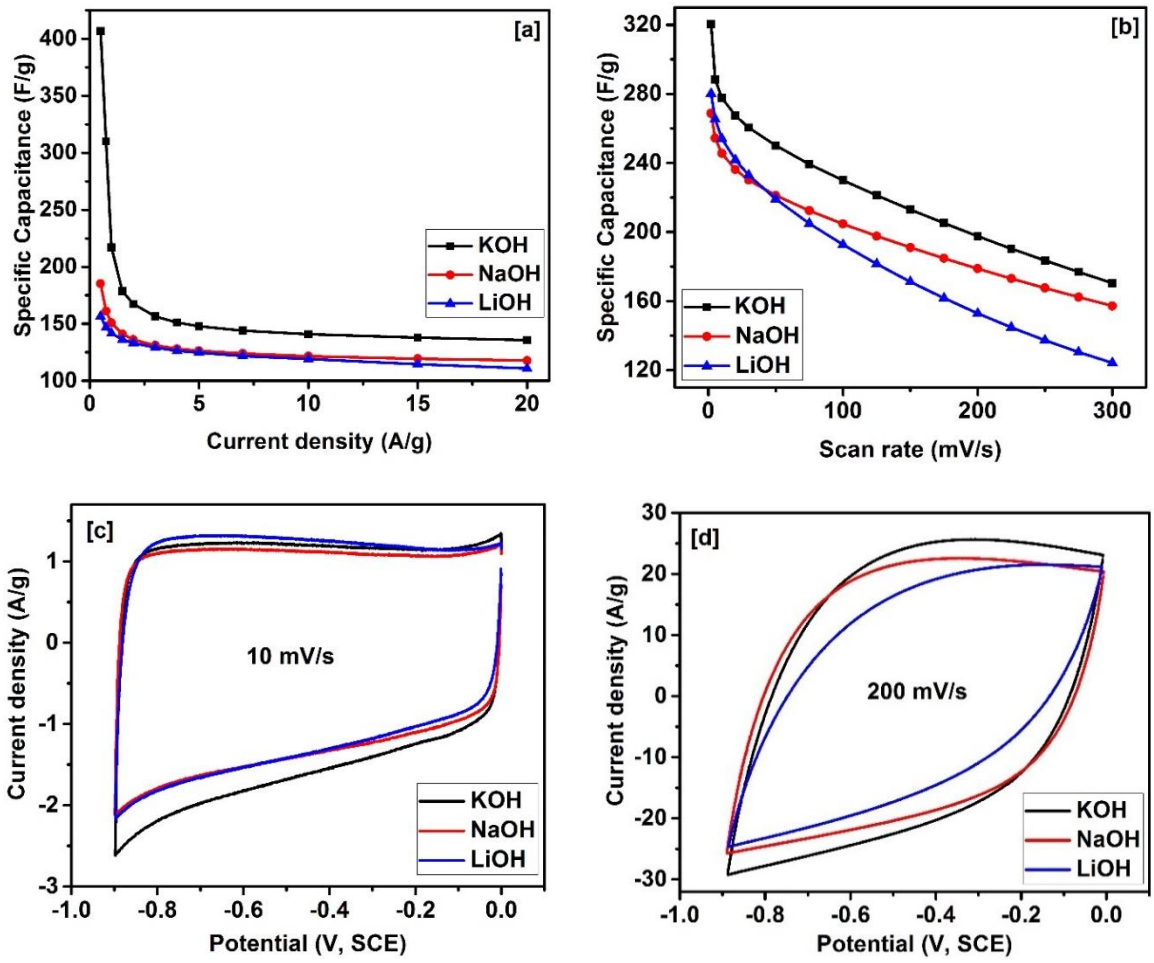

Figure 3.8 (a) Specific capacitances at different current densities, (b) Specific capacitances at various scan rates, and CV curves at the scan rates of (a) 10 mV/s and (b) 200 mV/s of OPAC-1 in 3M KOH, NaOH and LiOH electrolytes

Additionally, electrochemical impedance spectra were conducted to understand the electrochemical behavior of OPAC-1 in three different electrolytes. Figure 3.9a shows the Nyquist plots of OPAC-1 electrode in 3M KOH, NaOH and LiOH in a frequency range from 10 kHz to 0.05 Hz. Nyquist plots in three electrolytes had a similar shape, a modest semi-circle at mid to high frequency range, and straight line at low frequency. Interception at the real axis in the high frequency (inset Figure 3.9a) was an indication of the solution resistance [138]. The corresponding values for the solution resistance (R_S) were 0.83, 0.58 and 0.36 Ω for LiOH, NaOH, and KOH, respectively. Therefore, the KOH electrolyte had

better conductivity than NaOH and LiOH electrolytes. The diameter of the semi-circle represented the charge transfer resistance at the double layer [77], which was decreasing in the following sequence, LiOH > NaOH > KOH. The lowest charge transfer resistance value in KOH electrolyte suggests that K^+ contributed to an efficient charge adsorption-desorption process on the electrode-electrolyte interface due to its smaller hydrated ionic radius [139]. At a low frequency range, a near vertical straight line for KOH electrolyte can be observed, indicating a perfect capacitive behavior and efficient ionic diffusion process. Equivalent circuit was simulated using the EIS data to obtain the quantitative value for each electrochemical component of the electrode. The equivalent circuit and parameters of the OPAC-1 in three electrolytes are given in the Figure 3.9b. The equivalent circuit included the components related to solution resistance (R_S), charge transfer resistance (R_{CT}), constant phase elements (Q_1 and Q_2), and capacitance (C). Existence of the constant phase elements in the electrode can be attributed to capacitance of the double layer and the chaotic nature of the diffusion process or irregularities in electrode-electrolyte interface [140]. According to the simulated values total capacitance in three electrolytes increased in the order of LiOH < NaOH < KOH, which was consistent with the charge storage capacitance calculated from GCD and CV measurements (in Figure 3.8a,b). Bode plots (frequency vs. impedance) of three different electrolytes further confirmed the outstanding rate capability in KOH electrolyte (Figure 3.9c). At low frequency range (<1 Hz), the difference between the impedances in the three electrolytes were insignificant. Beyond the frequency of 1 Hz, a low impedance was observed for KOH compared to the NaOH and LiOH, indicating an excellent rate capability in KOH electrolyte.

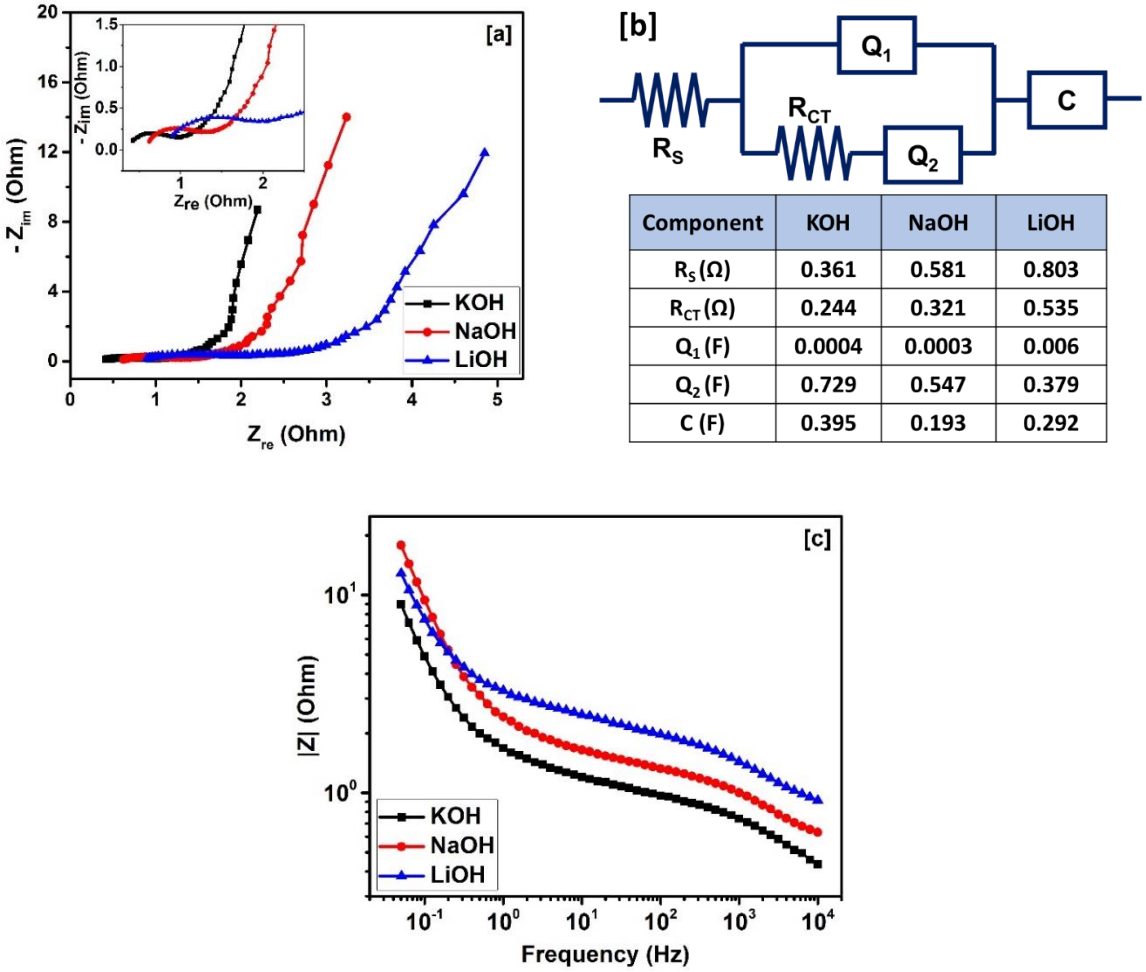

Component	KOH	NaOH	LiOH
R_S (Ω)	0.361	0.581	0.803
R_{CT} (Ω)	0.244	0.321	0.535
Q_1 (F)	0.0004	0.0003	0.006
Q_2 (F)	0.729	0.547	0.379
C (F)	0.395	0.193	0.292

Figure 3.9 (a) Nyquist plots with inset displaying magnification at higher frequency region, (b) Equivalent circuit obtained from simulating the EIS data and fitting values for the components of the equivalent circuit, and (c) Bodes plots of frequency vs impedance for OPAC-1 electrode in 3M KOH, NaOH LiOH electrolytes

OPAC-1 produced the optimum specific capacitance of 407 F/g at 0.5 A/g in 3M KOH electrolyte. However, reduction in specific capacitance with increasing current density was noticed. This was an effect of limited electrolyte ions diffusion to the micropores and a decreased amount of electrolyte ions accumulated on the electrode surface, owing to insufficient time at higher current densities [77,141]. Specific capacitance for OPAC-1 electrode was superior or comparable to the capacitance of previous biomass derived electrodes. Table 3.2 displays the capacitive performance of the

recently synthesized activated carbon from the biomass precursors. It should be noted that charge storage capacity of OPAC-1 was higher than commercially available activated carbons (< 200 F/g) [55], and even comparable to the more advanced forms of carbons such as graphene-based materials (100-347 F/g) [142], nitrogen doped graphene (138-326 F/g) [143], and CNT (128-335 F/g) [144]. The high capacitive performance of our material can be attributed to higher specific surface area, along with the prominent mesopore structure with 3-4 nm pore size in activated orange peel carbon. This provided larger surface for adsorption-desorption process of the ions and efficient pathways to ion transfer.

Table 3.2 Comparison of the orange peel derived carbon to carbon derived from other biomass precursors

Carbon Source	**BET Surface Area (m^2/g)**	**Specific Capacitance (F/g)**	**Current Density (A/g)**	**Electrolyte**	**Ref.**
Pitch	2602	263	0.05	6M KOH	[145]
Porous starch	3251	304	0.05	6M KOH	[146]
Celtuce leaves	3404	421	0.5	2M KOH	[147]
Sago bark	58	113	0.02	5M KOH	[148]
Corn straw	1413	379	0.05	6M KOH	[149]
Bamboo	3061	258	0.1	6M KOH	[73]
Oil palm kernel shell	462	210	0.5	1M KOH	[68]
Rice husk	2696	147	0.1	6M KOH	[61]
Ramie	1616	287	0.05	6M KOH	[80]
Camellia oleifera shell	1935	266	0.2	6M KOH	[150]
Soybean residue	1950	261	0.2	1M H_2SO_4	[151]
Neem dead leaves	1230	400	0.5	1M H_2SO_4	[135]
Orange peel	**1391**	**407**	**0.5**	**3M KOH**	**This work**

3.2.3 Electrochemical Properties of Orange Peel based Supercapacitor

Considering the high electrochemical performance of the OPAC-1, a symmetric supercapacitor was fabricated by assembling two OPAC-1 electrodes as the negative and positive electrodes. CV measurements were performed between 0 to 1 V in 3M KOH electrolyte for various scan rates (Figure 3.10a). The OPAC-1 based supercapacitor exhibited rectangular shaped CV curves at low scan rates and continued to maintain a rectangular shape without major distortion with increasing scan rate, indicating its suitability as a fast charge-discharge supercapacitor device. Charge storage process of an energy storage device can be identified by power law equation below.

$$i = av^b \quad \ldots (3.7)$$

where, i is the peak current (mA), v is the scan rate (V/s), and a and b are coefficients. Value for coefficient b determines whether the charge storage mechanism is either capacitive (b=1) or semi-infinite diffusion controlled (b=0.5) [152,153]. The logarithms of discharge current density vs logarithms of scan rate were plotted (Figure 3.10b) and 0.89 was obtained for the coefficient b. This suggests that charge storage process of the OPAC-1 supercapacitor was based on accumulation of electrical charges at electrode-electrolyte interface.

GCD profiles for OPAC-1 supercapacitor at different current densities in Figure 3.10c resemble a quasi-triangle shape, further confirming the formation of EDL during the charge storage process. IR drop for the supercapacitor was negligible even for higher current densities, which provided evidence for the minimum internal resistance of the device. The highest specific capacitance of 1728 mF/cm^2 was observed for the device at scan rate of 2 mV/s (Figure 3.10d). Figure 3.10e shows the specific capacitance of OPAC-

1 based supercapacitor at various current densities. The specific capacitance of the supercapacitor decreased from 729 to 697 mF/cm^2 as the current density increased from 2 to 14 mA/cm^2, demonstrating an impressive capacitance retention of 96 % across the same current density range. This further confirmed the high rate capability of the OPAC-1 supercapacitor. The well-developed structure of OPAC-1 facilitated the high rate capability by providing an unhindered pathway to ion transfer.

Energy and power density of the OPAC-1 supercapacitor is illustrated using a Ragone plot in Figure 3.10f. The supercapacitor delivered energy density between 100.4 to 93.4 mWh/cm^2 for the corresponding power density from 0.99 to 6.87 W/cm^2, while maintaining 93% from its highest energy density. These values were compared to previously reported supercapacitors based on other forms of carbons (inset Figure 3.10f). For example, energy and power performance of polyaniline deposited CNT (50.98 μWh/cm^2 at 28.404 mW/cm^2) [154], graphene oxide-polypyrrole composite (16.8 μWh/cm^2 at 0.08 mW/cm^2) [155], polypyrrole-MnO_2-CNT coated cotton thread (33 μWh/cm^2 at 0.67 mW/cm^2) [156], CNT coated carbon microfiber (9.8 μWh/cm^2 at 0.189 mW/cm^2) [157], and graphene-cellulose paper (1.5 μWh/cm^2 at 0.01 mW/cm^2) [158] were inferior to our work. High power capability of OPAC-1 supercapacitor indicates its potential for applications where rapid release of energy is required.

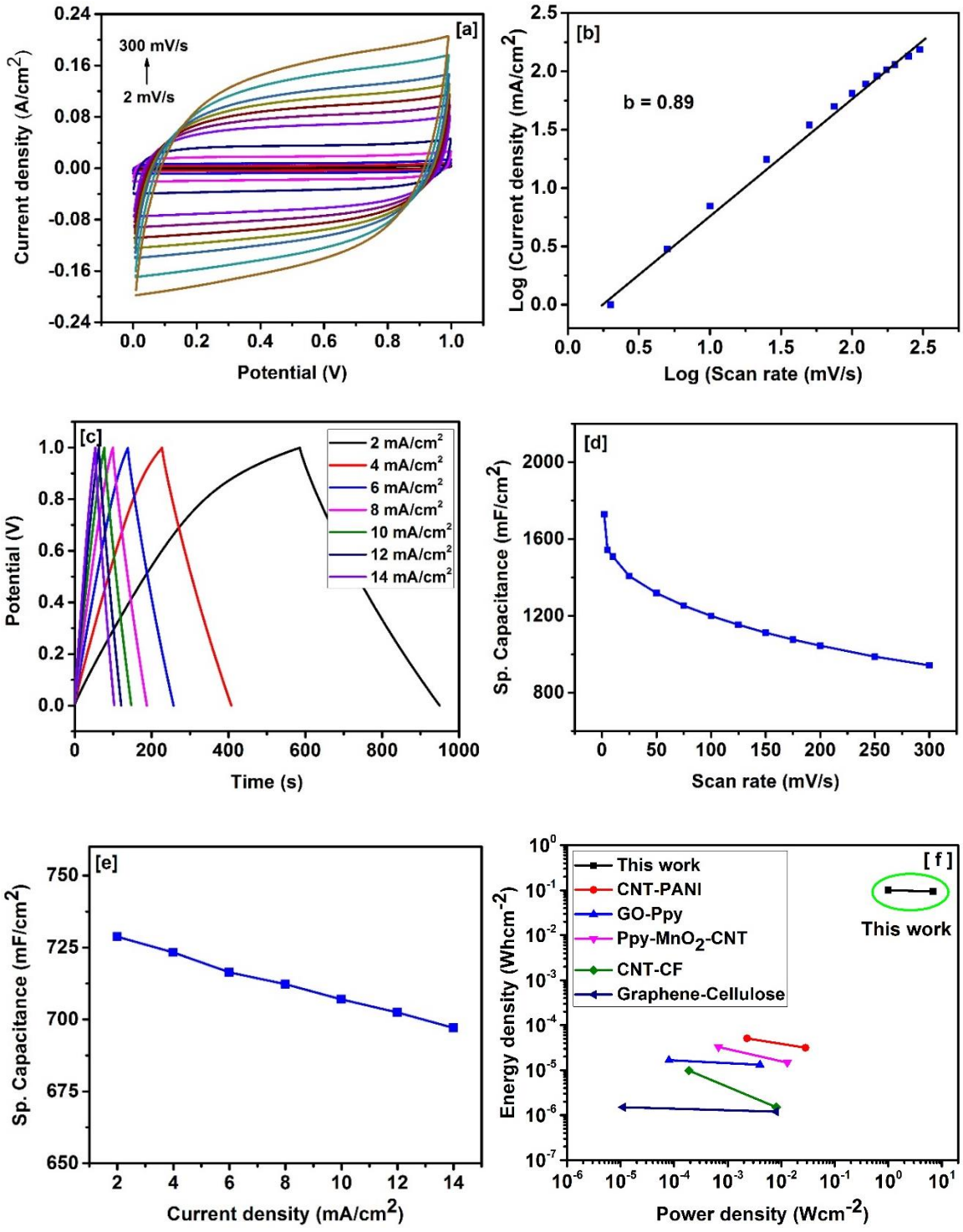

Figure 3.10 (a) CV curves at various scan rates, (b) log (discharge current density) vs log (scan rate) plot obtained using discharge current densities at 0.5 V from the CV curves at various scan rates, (c) GCD profiles at different current densities, (d) specific capacitances at different current densities of supercapacitor based on OPAC-1 in 3M KOH electrolyte, and (f) Ragone plot comparing OPAC-1 to previous reports

The temperature dependence of the OPAC-1 supercapacitor was studied by performing electrochemical measurements in the temperature range between 10 to 80 ^{o}C. Figure 3.11a displays the CV curves at 100 mV/s for various temperatures. The near rectangular shaped CV curves were observed even for the higher temperatures, indicating retention of the ideal EDL behavior and its excellent stability in a broad temperature range. Figure 3.11b shows GCD profiles of supercapacitor at a current density of 10 mA/cm^2 for different temperatures. The discharge time continued to increase as the temperature increased from 10 to 80 ^{o}C. As a result, charge storage capacity improved. The change in the capacitance at each temperature relative to capacitance at 10 ^{o}C was calculated (Figure 3.11c). A nearly 34% improvement in the capacitance was observed with the temperature increased from 10 to 80 ^{o}C at both current densities of 10 and 14 mA/cm^2.

To investigate the temperature dependence of the charge storage process, EIS measurements were performed at different temperatures. Figure 3.11d compares the Nyquist plots of OPAC-1 supercapacitor, measured at 10, 20, 40 and 70 ^{o}C. The features of the Nyquist plots, i.e. interception at real axis in high frequency region, diameter of the semi-circle at mid-high frequency region, and length of the straight line at low frequency range were associated with ohmic resistance of the solution, charge transfer resistance at electrode-electrolyte interface, and ion diffusion resistance, respectively. All of these parameters decreased with the increased in temperature. The decreased in the series resistance was a result of enhanced kinetic activity of electrolyte ions at elevated temperatures, rather than change in the electrical properties of electrode material [159]. Increased mobility of electrolyte ions caused the 34% increment in the capacitance value with increasing temperature. Figure 3.11e shows the Bode impedance plots at 10, 20, 40

and 70 ^{o}C of OPAC-1 device. It was noted that the impedances below 1 Hz were almost equal for the considered temperatures, while for the frequencies above 1 Hz, the impedance reduced faster with increasing temperature. These observations suggested that supercapacitor based on pyrolyzed orange peel induced superior electrochemical performance at elevated temperatures.

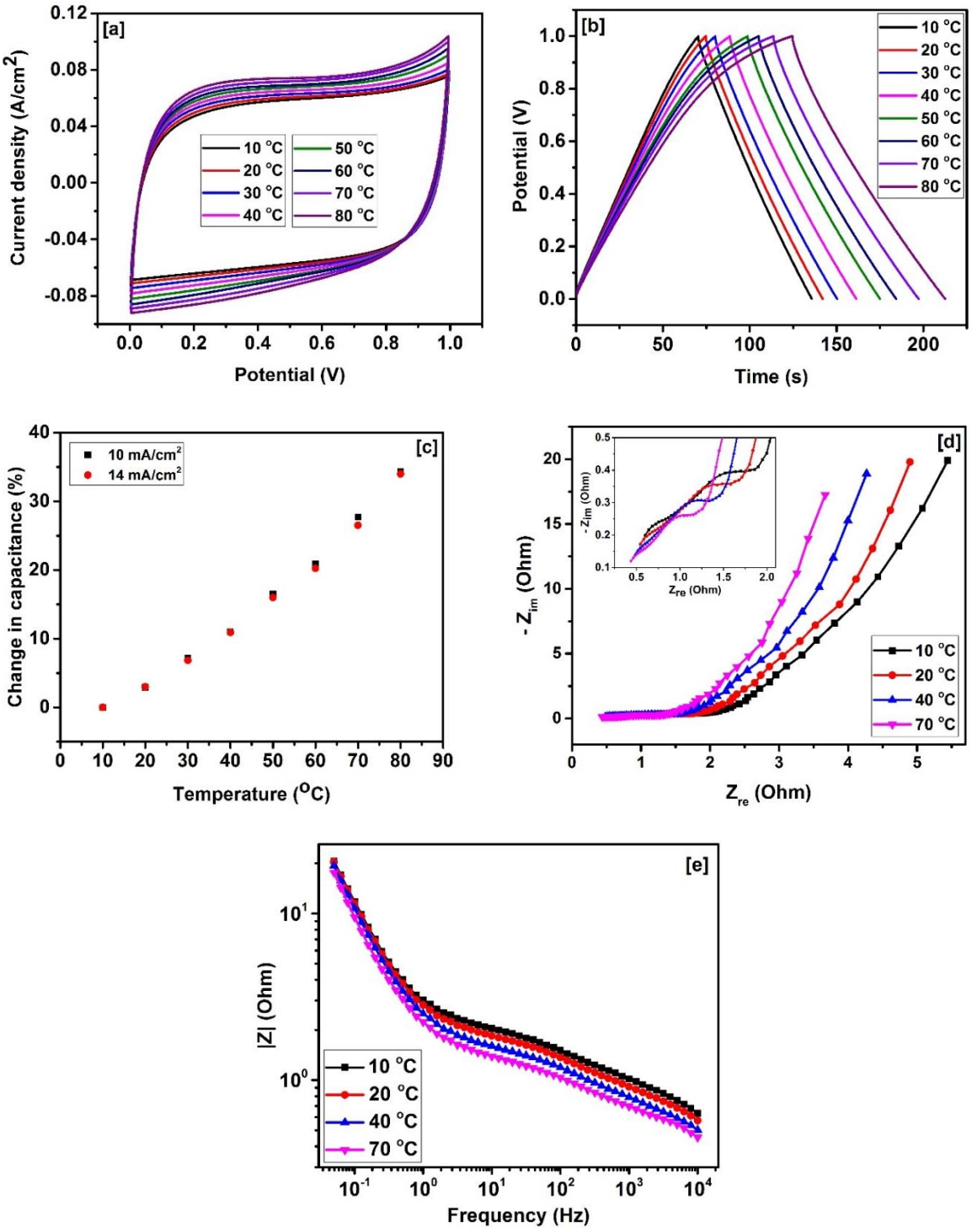

Figure 3.11 (a) CV curves for various temperatures at the scan rate of 100 mV/s, (b) GCD profiles for various temperatures at the current density of 10 mA/cm2, (c) % change of the specific capacitance against temperature, (d) Nyquist plots with inset displaying magnification at higher frequency region, and (e) Bodes plots of frequency vs impedance for OPAC-1 supercapacitor in 3 M KOH electrolyte

3.3 Summary

Sustainable and renewable carbon with well-developed porous structure was synthesized via simple pyrolysis and chemical activation from readily available waste orange peel. A higher mass ratio of activation agent produced carbon with a larger surface area and a higher micropore fraction. However, it was found that carbon with mesopores and suitable pore size contribute to the higher capacitive performance. Among the studied alkaline electrolytes, these carbon materials exhibited optimum charge storage and rate capability in KOH electrolyte, along with 108% capacitance retention over 5,000 cycles and identical electrochemical performance in different bending angles, indicating its potential as a stable and flexible electrode material. The prepared supercapacitor device showed superior energy density (100.4 mWh/cm^2) and power density (6.87 W/cm^2), improved temperature performance and negligible IR drop, owing to a suitable pore size and a higher degree of graphitization. This work presents the creation of proper electrode architecture and selection of an efficient electrolyte system to enhance the charge storage capacity of biowaste derived activated carbon for high performance, sustainable, and cost effective energy storage.

CHAPTER IV

4.0 CONCLUSIONS AND FUTURE WORKS

4.1 Conclusions

Limonene, an extract from orange peel, allowed the synthesis of bio-based polyol with a simple chemical route, which was readily utilized for the preparation of green polyurethane rigid foams. The prepared polyurethane rigid foams were suitable for thermal insulation applications due to the industrially acceptable density around 35 kg/m^3, excellent closed cell content over 90%, and higher compressive strength around 230 kPa. Inclusion of DMMP eliminated the fire risk and made these green PU foams even safer to use by reducing the burning time of neat PU foam by 83%.

Carbon based electrode material were easily synthesized by using orange peel waste, providing an alternative resource for petrochemical derived carbon. Chemical treatment of these bio-based carbon modified the graphitization, surface area, and pore volume. These modifications guided the selection of an optimum structure of carbon to achieve maximum charge storage capacitance, along with the selection of suitable electrolyte. OP derived carbon manifested high charge storage capacity, very high energy and power density, perfect long term cyclic stability, excellent rate behavior, suitability for flexible energy storage devices, and improved performance at elevated temperatures. In

summary, this thesis introduces a novel renewable resource and strategies to improve the efficiency of this renewable resource.

4.2 Future Works

The "Click" chemistry concept categorizes a set of reactions which produce high yield, employ uncomplicated reaction conditions, and are completed within a shorter time frame [160]. Synthesis of limonene polyol via thiol-ene coupling demonstrated some characteristics features of "click" chemistry. However, reaction time and yield can be further improved by adjusting the initiation conditions. In addition, combining limonene with thiol compounds having different number of alcohol groups can vary the hydroxyl number of the resultant polyols and subsequently the properties of PU foams.

One of the remarkable achievement of this work was the substantial improvement in fire resistance of the rigid PU foams due to the addition of DMMP. During the long-term use of foams, additives such as DMMP tends to leach out. This can be avoided by reactively attaching phosphorous containing compounds to the polyurethane network, opening a new area of research.

In this work, capacitive performance of the carbon electrode was achieved solely on formation of the EDL. Incorporation of pseudocapacitive behavior might be beneficial to improve the capacitive performance. Pseudocapacitance can be accomplished by either functionalizing the activated carbon or incorporating a metal oxide. Designing of a proper mixed system to improve the capacitance of bio-based carbon can be an interesting research topic.

Here, three different types of aqueous electrolytes were used. However, the potential window for the aqueous electrolytes are limited to 1.2 V, which invariably

reduced the charge storage capacity, whereas organic electrolytes offer a higher operating potential window and possibility of higher electrochemical performance.

REFERENCES

(1) Maher, K. D.; Bressler, D. C. Pyrolysis of Triglyceride Materials for the Production of Renewable Fuels and Chemicals. *Bioresour. Technol*. **2007**, 2351–2368.

(2) Belgacem, M. N.; Gandini, A. *Polymers and Composites from Renewable Resources*; Elsevier, 2008.

(3) Okkerse, C.; van Bekkum, H. From Fossil to Green. *Green Chem.* **1999**, *1* (2), 107–114.

(4) Lichtenthaler, F. W.; Peters, S. Carbohydrates as Green Raw Materials for the Chemical Industry. *C. R. Chim*. **2004**, *7* (2), 65–90.

(5) Mohanty, A. K.; Misra, M.; Drzal, L. T. Sustainable Bio-Composites from Renewable Resources: Opportunities and Challenges in the Green Materials World. *J. Polym. Environ.* **2002**, *10* (1–2), 19–26.

(6) Szycher, M. *Handbook of Polyurethanes*; CardioTech International Inc.: Woburn, MA , 1999.

(7) Petrović, Z. S.; Ferguson, J. Polyurethane Elastomers. *Prog. Polym. Sci.* **1991**, *16* (5), 695–836.

(8) Nohra, B.; Candy, L.; Blanco, J.-F.; Guerin, C.; Raoul, Y.; Mouloungui, Z. From Petrochemical Polyurethanes to Biobased Polyhydroxyurethanes. *Macromolecules* **2013**, *46* (10), 3771–3792.

(9) Lee, C. S.; Ooi, T. L.; Chuah, C. H.; Ahmad, S. Rigid Polyurethane Foam Production from Palm Oil-Based Epoxidized Diethanolamides. *J. Am. Oil Chem. Soc.* **2007**, *84* (12), 1161–1167.

(10) Thirumal, M.; Khastgir, D.; Singha, N. K.; Manjunath, B. S.; Naik, Y. P. Effect of Foam Density on the Properties of Water Blown Rigid Polyurethane Foam. *J. Appl. Polym. Sci.* **2008**, *108* (3), 1810–1817.

(11) Ionescu, M. *Chemistry and Technology of Polyols for Polyurethanes*; iSmithers Rapra Publishing: Shropshire, U.K., **2005**.

(12) Çaylı, G.; Küsefoğlu, S. Biobased Polyisocyanates from Plant Oil Triglycerides: Synthesis, Polymerization, and Characterization. *J. Appl. Polym. Sci.* **2008**, *109* (5), 2948–2955.

(13) Hojabri, L.; Kong, X.; Narine, S. S. Fatty Acid-Derived Diisocyanate and Biobased Polyurethane Produced from Vegetable Oil: Synthesis, Polymerization, and Characterization. *Biomacromolecules* **2009**, *10* (4), 884–891.

(14) Guo, A.; Javni, I.; Petrovic, Z. Rigid Polyurethane Foams Based on Soybean Oil. *J. Appl. Polym. Sci.* **2000**, *77* (2), 467–473.

(15) John, J.; Bhattacharya, M.; Turner, R. B. Characterization of Polyurethane Foams

from Soybean Oil. *J. Appl. Polym. Sci.* **2002**, *86* (12), 3097–3107.

(16) Tan, S.; Abraham, T.; Ference, D.; Macosko, C. W. Rigid Polyurethane Foams from a Soybean Oil-Based Polyol. *Polymer.* **2011**, *52* (13), 2840–2846.

(17) Yeganeh, H.; Mehdizadeh, M. R. Synthesis and Properties of Isocyanate Curable Millable Polyurethane Elastomers Based on Castor Oil as a Renewable Resource Polyol. *Eur. Polym. J.* **2004**, *40* (6), 1233–1238.

(18) Corcuera, M. A.; Rueda, L.; Fernandez d'Arlas, B.; Arbelaiz, A.; Marieta, C.; Mondragon, I.; Eceiza, A. Microstructure and Properties of Polyurethanes Derived from Castor Oil. *Polym. Degrad. Stab.* **2010**, *95* (11), 2175–2184.

(19) Rojek, P.; Prociak, A. Effect of Different Rapeseed-Oil-Based Polyols on Mechanical Properties of Flexible Polyurethane Foams. *J. Appl. Polym. Sci.* **2012**, *125* (4), 2936–2945.

(20) Fridrihsone, A.; Stirna, U.; Lazdiņa, B.; Misāne, M.; Vilsone, D. Characterization of Polyurethane Networks Structure and Properties Based on Rapeseed Oil Derived Polyol. *Eur. Polym. J.* **2013**, *49* (6), 1204–1214.

(21) Tanaka, R.; Hirose, S.; Hatakeyama, H. Preparation and Characterization of Polyurethane Foams Using a Palm Oil-Based Polyol. *Bioresour. Technol.* **2008**, *99* (9), 3810–3816.

(22) Badri, K. H.; Othman, Z.; Ahmad, S. H. Rigid Polyurethane Foams from Oil Palm Resources. *J. Mater. Sci.* **2004**, *39* (16/17), 5541–5542.

(23) Dwan'isa, J.-P. L.; Mohanty, A. K.; Misra, M.; Drzal, L. T.; Kazemizadeh, M. Novel Soy Oil Based Polyurethane Composites: Fabrication and Dynamic Mechanical Properties Evaluation. *J. Mater. Sci.* **2004**, *39* (5), 1887–1890.

(24) Guo, A.; Cho, Y.; Petrovi?, Z. S. Structure and Properties of Halogenated and Nonhalogenated Soy-Based Polyols. *J. Polym. Sci. Part A Polym. Chem.* **2000**, *38* (21), 3900–3910.

(25) Ionescu, M.; Petrović, Z. S.; Wan, X. Ethoxylated Soybean Polyols for Polyurethanes. *J. Polym. Environ.* **2010**, *18* (1), 1–7.

(26) Guo, A.; Demydov, D.; Zhang, W.; Petrovic, Z. S. Polyols and Polyurethanes from Hydroformylation of Soybean Oil. *J. Polym. Environ.* **2002**, *10* (1/2), 49–52.

(27) Khoe, T. H.; Otey, F.; Frankel, E. N.; Cowan, J. C. Polyurethane Foams from Hydroxymethylated Fatty Diethanolamides. *J. Am. Oil Chem. Soc.* **1973**, *50* (8), 331–333.

(28) Lyon, C. K.; Garrett, V. H.; Frankel, E. N. Rigid Urethane Foams from Hydroxymethylated Castor Oil, Safflower Oil, Oleic Safflower Oil, and Polyol Esters of Castor Acids. *J. Am. Oil Chem. Soc.* **1974**, *51* (8), 331–334.

(29) Tran, P.; Graiver, D.; Narayan, R. Ozone-Mediated Polyol Synthesis from Soybean Oil. *J. Am. Oil Chem. Soc.* **2005**, *82* (9), 653–659.

(30) Petrović, Z. S.; Zhang, W.; Javni, I. Structure and Properties of Polyurethanes Prepared from Triglyceride Polyols by Ozonolysis. *Biomacromolecules* **2005**, *6* (2), 713–719.

(31) Desai, S. D.; Patel, J. V.; Sinha, V. K. Polyurethane Adhesive System from Biomaterial-Based Polyol for Bonding Wood. *Int. J. Adhes. Adhes.* **2003**, *23* (5), 393–399.

(32) Petrović, Z. S.; Cvetković, I.; Hong, D.; Wan, X.; Zhang, W.; Abraham, T.; Malsam, J. Polyester Polyols and Polyurethanes from Ricinoleic Acid. *J. Appl. Polym. Sci.* **2008**, *108* (2), 1184–1190.

(33) Kade, M. J.; Burke, D. J.; Hawker, C. J. The Power of Thiol-Ene Chemistry. *J. Polym. Sci., Part A: Polym. Chem.* **2010**, *48* (4), 743–750.

(34) Bexell, U.; Olsson, M.; Johansson, M.; Samuelsson, J.; Sundell, P.-E. A Tribological Study of a Novel Pre-Treatment with Linseed Oil Bonded to Mercaptosilane Treated Aluminium. *Surf. Coat. Technol.* **2003**, *166* (2), 141–152.

(35) Sharma, B. K.; Adhvaryu, A.; Erhan, S. Z. Synthesis of Hydroxy Thio-Ether Derivatives of Vegetable Oil. *J. Agric. Food Chem.* **2006**, *54* (26), 9866–9872.

(36) Sharma, B. K.; Adhvaryu, A.; Erhan, S. Z. Friction and Wear Behavior of Thioether Hydroxy Vegetable Oil. *Tribol. Int.* **2009**, *42* (2), 353–358.

(37) Black, M.; Rawlins, J. W. Thiol–ene UV-Curable Coatings Using Vegetable Oil Macromonomers. *Eur. Polym. J.* **2009**, *45* (5), 1433–1441.

(38) Lluch, C.; Ronda, J. C.; Galià, M.; Lligadas, G.; Cádiz, V. Rapid Approach to Biobased Telechelics through Two One-Pot Thiol−Ene Click Reactions. *Biomacromolecules* **2010**, *11* (6), 1646–1653.

(39) Samuelsson, J.; Jonsson, M.; Brinck, T.; Johansson, M. Thiol-Ene Coupling Reaction of Fatty Acid Monomers. *J. Polym. Sci., Part A: Polym. Chem.* **2004**, *42* (24), 6346–6352.

(40) Lluch, C.; Lligadas, G.; Ronda, J. C.; Galià, M.; Cadiz, V. "Click" Synthesis of Fatty Acid Derivatives as Fast-Degrading Polyanhydride Precursors. *Macromol. Rapid Commun.* **2011**, *32* (17), 1343–1351.

(41) Türünç, O.; Meier, M. A. R. Fatty Acid Derived Monomers and Related Polymers Via Thiol-Ene (Click) Additions. *Macromol. Rapid Commun.* **2010**, *31* (20), 1822–1826.

(42) Türünç, O.; Meier, M. A. R.; Hofmann, D.; Entrialgo-Castaño, M.; Kratz, K.; Lendlein, A.; Sokolsky-Papkov, M.; Shikanov, A.; Kumar, N.; Vaisman, B.; et al. Thiol-Ene vs. ADMET: A Complementary Approach to Fatty Acid-Based Biodegradable Polymers. *Green Chem.* **2011**, *13* (2), 314.

(43) Zammarano, M.; Krämer, R. H.; Harris, R.; Ohlemiller, T. J.; Shields, J. R.; Rahatekar, S. S.; Lacerda, S.; Gilman, J. W. Flammability Reduction of Flexible Polyurethane Foams via Carbon Nanofiber Network Formation. *Polym. Adv.*

Technol. **2008**, *19* (6), 588–595.

(44) Benrashid, R.; Nelson, G. L. Synthesis of New Siloxane Urethane Block Copolymers and Their Properties. *J. Polym. Sci., Part A: Polym. Chem.* **1994**, *32* (10), 1847–1865.

(45) Xing, W.; Yuan, H.; zhang, P.; Yang, H.; Song, L.; Hu, Y. Functionalized Lignin for Halogen-Free Flame Retardant Rigid Polyurethane Foam: Preparation, Thermal Stability, Fire Performance and Mechanical Properties. *J. Polym. Res.* **2013**, *20* (9), 234.

(46) Gharehbaghi, A.; Bashirzadeh, R.; Ahmadi, Z. Polyurethane Flexible Foam Fire Resisting by Melamine and Expandable Graphite: Industrial Approach. *J. Cell. Plast.* **2011**, *47* (6), 549–565.

(47) König, A.; Malek, A.; Fehrenbacher, U.; Brunklaus, G.; Wilhelm, M.; Hirth, T. Silane-Functionalized Flame-Retardant Aluminum Trihydroxide in Flexible Polyurethane Foam. *J. Cell. Plast.* **2010**, *46* (5), 395–413.

(48) Chen, M.-J.; Chen, C.-R.; Tan, Y.; Huang, J.-Q.; Wang, X.-L.; Chen, L.; Wang, Y.-Z. Inherently Flame-Retardant Flexible Polyurethane Foam with Low Content of Phosphorus-Containing Cross-Linking Agent. *Ind. Eng. Chem. Res.* **2014**, *53* (3), 1160–1171.

(49) Beidaghi, M.; Gogotsi, Y.; Wang, Z. L.; Akyildiz, I. F.; Su, W.; Sankarasubramaniam, Y.; Cayirci, E.; Wang, Z. L.; Wu, W.; Wang, Z. L.; et al. Capacitive Energy Storage in Micro-Scale Devices: Recent Advances in Design and Fabrication of Micro-Supercapacitors. *Energy Environ. Sci.* **2014**, *7* (3), 867.

(50) Merlet, C.; Rotenberg, B.; Madden, P. A.; Taberna, P.-L.; Simon, P.; Gogotsi, Y.; Salanne, M. On the Molecular Origin of Supercapacitance in Nanoporous Carbon Electrodes. *Nat. Mater.* **2012**, *11* (4), 306–310.

(51) Botte, G. G.; Muthuvel, M. Electrochemical Energy Storage: Applications, Processes, and Trends. In *Handbook of Industrial Chemistry and Biotechnology*; Springer US: Boston, MA, 2012; pp 1497–1539.

(52) Choi, N.-S.; Chen, Z.; Freunberger, S. A.; Ji, X.; Sun, Y.-K.; Amine, K.; Yushin, G.; Nazar, L. F.; Cho, J.; Bruce, P. G. Challenges Facing Lithium Batteries and Electrical Double-Layer Capacitors. *Angew. Chem. Int. Ed.* **2012**, *51* (40), 9994–10024.

(53) Dyatkin, B.; Presser, V.; Heon, M.; Lukatskaya, M. R.; Beidaghi, M.; Gogotsi, Y. Development of a Green Supercapacitor Composed Entirely of Environmentally Friendly Materials. *ChemSusChem* **2013**, *6* (12), 2269–2280.

(54) Chen, T.; Dai, L. Flexible Supercapacitors Based on Carbon Nanomaterials. *J. Mater. Chem. A* **2014**, *2* (28), 10756.

(55) Divyashree, A..; Hegde, G. Activated Carbon Nanospheres Derived from Bio-Waste Materials for Supercapacitor Applications – a Review. *RSC Adv.* **2015**, *5* (107), 88339–88352.

(56) Pandolfo, A. G.; Hollenkamp, A. F. Carbon Properties and Their Role in Supercapacitors. *J. Power Sources* **2006**, *157* (1), 11–27.

(57) van Wyk, J. P. . Biotechnology and the Utilization of Biowaste as a Resource for Bioproduct Development. *Trends Biotechnol.* **2001**, *19* (5), 172–177.

(58) Hao, P.; Zhao, Z.; Tian, J.; Li, H.; Sang, Y.; Yu, G.; Cai, H.; Liu, H.; Wong, C. P.; Umar, A. Hierarchical Porous Carbon Aerogel Derived from Bagasse for High Performance Supercapacitor Electrode. *Nanoscale* **2014**, *6* (20), 12120–12129.

(59) Rufford, T. E.; Hulicova-Jurcakova, D.; Khosla, K.; Zhu, Z.; Lu, G. Q. Microstructure and Electrochemical Double-Layer Capacitance of Carbon Electrodes Prepared by Zinc Chloride Activation of Sugar Cane Bagasse. *J. Power Sources* **2010**, *195* (3), 912–918.

(60) Wahid, M.; Puthusseri, D.; Phase, D.; Ogale, S. Enhanced Capacitance Retention in a Supercapacitor Made of Carbon from Sugarcane Bagasse by Hydrothermal Pretreatment. *Energy Fuels* **2014**, *28* (6), 4233–4240.

(61) Teo, E. Y. L.; Muniandy, L.; Ng, E.-P.; Adam, F.; Mohamed, A. R.; Jose, R.; Chong, K. F. High Surface Area Activated Carbon from Rice Husk as a High Performance Supercapacitor Electrode. *Electrochim. Acta* **2016**, *192*, 110–119.

(62) Liu, D.; Zhang, W.; Lin, H.; Li, Y.; Lu, H.; Wang, Y. Hierarchical Porous Carbon Based on the Self-Templating Structure of Rice Husk for High-Performance Supercapacitors. *RSC Adv.* **2015**, *5* (25), 19294–19300.

(63) Gao, Y.; Li, L.; Jin, Y.; Wang, Y.; Yuan, C.; Wei, Y.; Chen, G.; Ge, J.; Lu, H. Porous Carbon Made from Rice Husk as Electrode Material for Electrochemical Double Layer Capacitor. *Appl. Energy* **2015**, *153*, 41–47.

(64) Qu, W.-H.; Xu, Y.-Y.; Lu, A.-H.; Zhang, X.-Q.; Li, W.-C. Converting Biowaste Corncob Residue into High Value Added Porous Carbon for Supercapacitor Electrodes. *Bioresour. Technol.* **2015**, *189*, 285–291.

(65) Sun, L.; Tian, C.; Li, M.; Meng, X.; Wang, L.; Wang, R.; Yin, J.; Fu, H. From Coconut Shell to Porous Graphene-like Nanosheets for High-Power Supercapacitors. *J. Mater. Chem. A* **2013**, *1* (21), 6462.

(66) Li, X.; Xing, W.; Zhuo, S.; Zhou, J.; Li, F.; Qiao, S.-Z.; Lu, G.-Q. Preparation of Capacitor's Electrode from Sunflower Seed Shell. *Bioresour. Technol.* **2011**, *102* (2), 1118–1123.

(67) Xiao, K.; Ding, L.-X.; Chen, H.; Wang, S.; Lu, X.; Wang, H. Nitrogen-Doped Porous Carbon Derived from Residuary Shaddock Peel: A Promising and Sustainable Anode for High Energy Density Asymmetric Supercapacitors. *J. Mater. Chem. A* **2016**, *4* (2), 372–378.

(68) Misnon, I. I.; Zain, N. K. M.; Aziz, R. A.; Vidyadharan, B.; Jose, R. Electrochemical Properties of Carbon from Oil Palm Kernel Shell for High Performance Supercapacitors. *Electrochim. Acta* **2015**, *174*, 78–86.

(69) Rufford, T. E.; Hulicova-Jurcakova, D.; Zhu, Z.; Lu, G. Q. Nanoporous Carbon Electrode from Waste Coffee Beans for High Performance Supercapacitors. Electrochem. Commun. **2008**; *10* (10), 1594-1597.

(70) Peng, C.; Yan, X.; Wang, R.; Lang, J.; Ou, Y.; Xue, Q. Promising Activated Carbons Derived from Waste Tea-Leaves and Their Application in High Performance Supercapacitors Electrodes. *Electrochim. Acta* **2013**, *87*, 401–408.

(71) Lv, Y.; Gan, L.; Liu, M.; Xiong, W.; Xu, Z.; Zhu, D.; Wright, D. S. A Self-Template Synthesis of Hierarchical Porous Carbon Foams Based on Banana Peel for Supercapacitor Electrodes. *J. Power Sources* **2012**, *209*, 152–157.

(72) Li, J.; Wu, Q. Water Bamboo-Derived Porous Carbons as Electrode Materials for Supercapacitors. *New J. Chem.* **2015**, *39* (5), 3859–3864.

(73) Yang, C.-S.; Jang, Y. S.; Jeong, H. K. Bamboo-Based Activated Carbon for Supercapacitor Applications. *Curr. Appl. Phys.* **2014**, *14* (12), 1616–1620.

(74) Zequine, C.; Ranaweera, C. K.; Wang, Z.; Singh, S.; Tripathi, P.; Srivastava, O. N.; Gupta, B. K.; Ramasamy, K.; Kahol, P. K.; Dvornic, P. R.; et al. High Per Formance and Flexible Supercapacitors Based on Carbonized Bamboo Fibers for Wide Temperature Applications. *Sci. Rep.* **2016**, *6*, 31704.

(75) Wang, H.; Xu, Z.; Kohandehghan, A.; Li, Z.; Cui, K.; Tan, X.; Stephenson, T. J.; King'ondu, C. K.; Holt, C. M. B.; Olsen, B. C.; et al. Interconnected Carbon Nanosheets Derived from Hemp for Ultrafast Supercapacitors with High Energy. *ACS Nano* **2013**, *7* (6), 5131–5141.

(76) Raymundo-Piñero, E.; Cadek, M.; Béguin, F. Tuning Carbon Materials for Supercapacitors by Direct Pyrolysis of Seaweeds. *Adv. Funct. Mater.* **2009**, *19* (7), 1032–1039.

(77) Chang, J.; Gao, Z.; Wang, X.; Wu, D.; Xu, F.; Wang, X.; Guo, Y.; Jiang, K. Activated Porous Carbon Prepared from Paulownia Flower for High Performance Supercapacitor Electrodes. *Electrochim. Acta* **2015**, *157*, 290–298.

(78) Biswal, M.; Banerjee, A.; Deo, M.; Ogale, S. From Dead Leaves to High Energy Density Supercapacitors. *Energy Environ. Sci.* **2013**, *6* (4), 1249.

(79) Cheng, P.; Li, T.; Yu, H.; Zhi, L.; Liu, Z.; Lei, Z. Biomass-Derived Carbon Fiber Aerogel as a Binder-Free Electrode for High-Rate Supercapacitors. *J. Phys. Chem. C* **2016**, *120* (4), 2079–2086.

(80) Du, X.; Zhao, W.; Wang, Y.; Wang, C.; Chen, M.; Qi, T.; Hua, C.; Ma, M. Preparation of Activated Carbon Hollow Fibers from Ramie at Low Temperature for Electric Double-Layer Capacitor Applications. *Bioresour. Technol.* **2013**, *149*, 31–37.

(81) Largeot, C.; Portet, C.; Chmiola, J.; Taberna, P. L.; Gogotsi, Y.; Simon, P. Relation between the Ion Size and Pore Size for an Electric Double-Layer Capacitor. *J. Am. Chem. Soc.* **2008**, *130* (9), 2730–2731.

(82) Wu, F.-C.; Tseng, R.-L.; Hu, C.-C.; Wang, C.-C. Effects of Pore Structure and Electrolyte on the Capacitive Characteristics of Steam- and KOH-Activated Carbons for Supercapacitors. *J. Power Sources* **2005**, *144* (1), 302–309.

(83) Valix, M.; Cheung, W. H.; McKay, G. Preparation of Activated Carbon Using Low Temperature Carbonisation and Physical Activation of High Ash Raw Bagasse for Acid Dye Adsorption. *Chemosphere* **2004**, *56* (5), 493–501.

(84) Guo, Y.; Zhang, H.; Tao, N.; Liu, Y.; Qi, J.; Wang, Z.; Xu, H. Adsorption of Malachite Green and Iodine on Rice Husk-Based Porous Carbon. *Mater. Chem. Phys.* **2003**, *82* (1), 107–115.

(85) Guo, Y.; Qi, J.; Jiang, Y.; Yang, S.; Wang, Z.; Xu, H. Performance of Electrical Double Layer Capacitors with Porous Carbons Derived from Rice Husk. *Mater. Chem. Phys.* **2003**, *80* (3), 704–709.

(86) Girgis, B. S.; El-Hendawy, A.-N. A. Porosity Development in Activated Carbons Obtained from Date Pits under Chemical Activation with Phosphoric Acid. *Microporous Mesoporous Mater.* **2002**, *52* (2), 105–117.

(87) Caturla, F.; Molina-Sabio, M.; Rodríguez-Reinoso, F. Preparation of Activated Carbon by Chemical Activation with ZnCl2. *Carbon* **1991**, *29* (7), 999–1007.

(88) Wang, J.; Kaskel, S. KOH Activation of Carbon-Based Materials for Energy Storage. *J. Mater. Chem.* **2012**, *22* (45), 23710.

(89) Maciá-Agulló, J. A.; Moore, B. C.; Cazorla-Amorós, D.; Linares-Solano, A. Activation of Coal Tar Pitch Carbon Fibres: Physical Activation vs. Chemical Activation. *Carbon* **2004**, *42* (7), 1367–1370.

(90) Raymundo-Piñero, E.; Leroux, F.; Béguin, F. A High-Performance Carbon for Supercapacitors Obtained by Carbonization of a Seaweed Biopolymer. *Adv. Mater.* **2006**, *18* (14), 1877–1882.

(91) Ferrero, G. A.; Fuertes, A. B.; Sevilla, M.; Choi, N.-S.; Frackowiak, E.; Beguin, F.; Beguin, F.; Presser, V.; Balducci, A.; Frackowiak, E.; et al. From Soybean Residue to Advanced Supercapacitors. *Sci. Rep.* **2015**, *5*, 16618.

(92) Li, Y.; Wang, G.; Wei, T.; Fan, Z.; Yan, P. Nitrogen and Sulfur Co-Doped Porous Carbon Nanosheets Derived from Willow Catkin for Supercapacitors. *Nano Energy* **2016**, *19*, 165–175.

(93) Foreign Agricultural Service/USDA. *Citrus: World Markets and Trade*; 2017.

(94) Grohmann, K.; Baldwin, E. A. Hydrolysis of Orange Peel with Pectinase and Cellulase Enzymes. *Biotechnol. Lett.* **1992**, *14* (12), 1169–1174.

(95) Marín, F. R.; Soler-Rivas, C.; Benavente-García, O.; Castillo, J.; Pérez-Alvarez, J. A. By-Products from Different Citrus Processes as a Source of Customized Functional Fibres. *Food Chem.* **2007**, *100* (2), 736–741.

(96) Widmer, W.; Zhou, W.; Grohmann, K. Pretreatment Effects on Orange Processing

Waste for Making Ethanol by Simultaneous Saccharification and Fermentation. *Bioresour. Technol.* **2010**, *101* (14), 5242–5249.

(97) Prakash Maran, J.; Sivakumar, V.; Thirugnanasambandham, K.; Sridhar, R. Optimization of Microwave Assisted Extraction of Pectin from Orange Peel. *Carbohydr. Polym.* **2013**, *97* (2), 703–709.

(98) Feng, N.; Guo, X.; Liang, S.; Zhu, Y.; Liu, J. Biosorption of Heavy Metals from Aqueous Solutions by Chemically Modified Orange Peel. *J. Hazard. Mater.* **2011**, *185* (1), 49–54.

(99) Khaled, A.; Nemr, A. El; El-Sikaily, A.; Abdelwahab, O. Removal of Direct N Blue-106 from Artificial Textile Dye Effluent Using Activated Carbon from Orange Peel: Adsorption Isotherm and Kinetic Studies. *J. Hazard. Mater.* **2009**, *165* (1), 100–110.

(100) Martín, M. A.; Siles, J. A.; Chica, A. F.; Martín, A. Biomethanization of Orange Peel Waste. *Bioresour. Technol.* **2010**, *101* (23), 8993–8999.

(101) Ranaweera, C. K.; Ionescu, M.; Bilic, N.; Wan, X.; Kahol, P. K.; Gupta, R. K. Biobased Polyols Using Thiol-Ene Chemistry for Rigid Polyurethane Foams with Enhanced Flame-Retardant Properties. *J. Renew. Mater.* **2017**, 1–12.

(102) Steuer, B.; Schulz, H.; Läger, E. Classification and Analysis of Citrus Oils by NIR Spectroscopy. *Food Chem.* **2001**, *72* (1), 113–117.

(103) Angel Siles López, J.; Li, Q.; Thompson, I. P. Biorefinery of Waste Orange Peel. *Crit. Rev. Biotechnol.* **2010**, *30* (1), 63–69.

(104) Modena, M.; Bates, R. B.; Marvel, C. S. Some Low Molecular Weight Polymers of D-Limonene and Related Terpenes Obtained by Ziegler-Type Catalysts. *J. Polym. Sci., Part A: Gen. Pap.* **1965**, *3* (3), 949–960.

(105) Doiuchi, T.; Yamaguchi, H.; Minoura, Y. Cyclocopolymerization of D-Limonene with Maleic Anhydride. *Eur. Polym. J.* **1981**, *17* (9), 961–968.

(106) Griesbaum, K. Problems and Possibilities of the Free-Radical Addition of Thiols to Unsaturated Compounds. *Angew. Chem. Int. Ed. English* **1970**, *9* (4), 273–287.

(107) Janes, J. F.; Marr, I. M.; Unwin, N.; Banthorpe, D. V.; Yusuf, A. Reaction of Monoterpenoids with Hydrogen Sulphide to Form Thiols Andepi-Sulphides of Potential Organoleptic Significance. *Flavour Fragrance J.* **1993**, *8* (5), 289–294.

(108) Marvel, C. S.; Olson, L. E. Polyalkylene Sulfides. XIII. Polymers from 4-Vinyl-1-Cyclohexene and D-Limonene. *J. Polym. Sci.* **1957**, *26* (112), 23–28.

(109) Chen, B.; Chen, Z. Sorption of Naphthalene and 1-Naphthol by Biochars of Orange Peels with Different Pyrolytic Temperatures. *Chemosphere* **2009**, *76* (1), 127–133.

(110) Arie, A. A.; Kristianto, H.; Lee, J. K. Activated Carbons from Orange Peel Waste as Supercapacitor Electrodes. *ECS Trans.* **2013**, *53* (31), 9–13.

(111) Dhelipan, M.; Arunchander, A.; Sahu, A. K.; Kalpana, D. Activated Carbon from

Orange Peels as Supercapacitor Electrode and Catalyst Support for Oxygen Reduction Reaction in Proton Exchange Membrane Fuel Cell. *J. Saudi Chem. Soc.* **2016**.

(112) Desroches, M.; Escouvois, M.; Auvergne, R.; Caillol, S.; Boutevin, B. From Vegetable Oils to Polyurethanes: Synthetic Routes to Polyols and Main Industrial Products. *Polym. Rev.* **2012**, *52* (1), 38–79.

(113) Wilbon, P. A.; Chu, F.; Tang, C. Progress in Renewable Polymers from Natural Terpenes, Terpenoids, and Rosin. *Macromol. Rapid Commun.* **2013**, *34* (1), 8–37.

(114) Widya, T.; Macosko, C. Nanoclay- Modified Rigid Polyurethane Foam. *J. Macromol. Sci., Part B: Phys.* **2005**, *44* (6), 897–908.

(115) Feng, F.; Qian, L. The Flame Retardant Behaviors and Synergistic Effect of Expandable Graphite and Dimethyl Methylphosphonate in Rigid Polyurethane Foams. *Polym. Compos.* **2014**, *35* (2), 301–309.

(116) Xi, W.; Qian, L.; Chen, Y.; Wang, J.; Liu, X. Addition Flame-Retardant Behaviors of Expandable Graphite and [bis(2-Hydroxyethyl)amino]-Methyl-Phosphonic Acid Dimethyl Ester in Rigid Polyurethane Foams. *Polym. Degrad. Stab.* **2015**, *122*, 36–43.

(117) Zlatanić, A.; Lava, C.; Zhang, W.; Petrović, Z. S. Effect of Structure on Properties of Polyols and Polyurethanes Based on Different Vegetable Oils. *J. Polym. Sci., Part B: Polym. Phys.* **2004**, *42* (5), 809–819.

(118) Liu, F.; Ding, X.; Su, Y. Properties of Rigid Polyurethane Foams Produced by the Addition of Phosphorus Compounds. *Am. J. Mater. Res.* **2014**, *1* (1), 14–19.

(119) Lorenzetti, A.; Modesti, M.; Besco, S.; Hrelja, D.; Donadi, S. Influence of Phosphorus Valency on Thermal Behaviour of Flame Retarded Polyurethane Foams. *Polym. Degrad. Stab.* **2011**, *96* (8), 1455–1461.

(120) Duquesne, S.; Le Bras, M.; Bourbigot, S.; Delobel, R.; Camino, G.; Eling, B.; Lindsay, C.; Roels, T.; Vezin, H. Mechanism of Fire Retardancy of Polyurethanes Using Ammonium Polyphosphate. *J. Appl. Polym. Sci.* **2001**, *82* (13), 3262–3274.

(121) Zhu, Y.; Murali, S.; Stoller, M. D.; Ganesh, K. J.; Cai, W.; Ferreira, P. J.; Pirkle, A.; Wallace, R. M.; Cychosz, K. A.; Thommes, M.; et al. Carbon-Based Supercapacitors Produced by Activation of Graphene. *Science.* **2011**, *332* (6037), 1537-1541.

(122) Gao, Y.; Li, L.; Jin, Y.; Wang, Y.; Yuan, C.; Wei, Y.; Chen, G.; Ge, J.; Lu, H. Porous Carbon Made from Rice Husk as Electrode Material for Electrochemical Double Layer Capacitor. *Appl. Energy* **2015**, *153*, 41–47.

(123) Cheng, P.; Li, T.; Yu, H.; Zhi, L.; Liu, Z.; Lei, Z. Biomass-Derived Carbon Fiber Aerogel as a Binder-Free Electrode for High-Rate Supercapacitors. *J. Phys. Chem. C* **2016**, *120* (4), 2079–2086.

(124) Wahid, M.; Puthusseri, D.; Phase, D.; Ogale, S. Enhanced Capacitance Retention in a Supercapacitor Made of Carbon from Sugarcane Bagasse by Hydrothermal

Pretreatment. *Energy Fuels* **2014**, *28* (6), 4233–4240.

(125) Brebu, M.; Vasile, C. THERMAL DEGRADATION OF LIGNIN – A REVIEW. *Cellul. Chem. Technol.* **2010**, *44* (9), 353–363.

(126) Paris, O.; Zollfrank, C.; Zickler, G. A. Decomposition and Carbonisation of Wood Biopolymers—a Microstructural Study of Softwood Pyrolysis. *Carbon* **2005**, *43* (1), 53–66.

(127) Kastanaki, E.; Vamvuka, D.; Grammelis, P.; Kakaras, E. Thermogravimetric Studies of the Behavior of Lignite–biomass Blends during Devolatilization. *Fuel Process. Technol.* **2002**, *77*, 159–166.

(128) Mi, J.; Wang, X.; Fan, R.; Qu, W.; Li, W. Coconut-Shell-Based Porous Carbons with a Tunable Micro / Mesopore Ratio for High-Performance Supercapacitors. *Energy Fuels* **2012**, *26* (8), 5321–5329.

(129) Li, Y.; Li, Z.; Shen, P. K. Simultaneous Formation of Ultrahigh Surface Area and Three-Dimensional Hierarchical Porous Graphene-Like Networks for Fast and Highly Stable Supercapacitors. *Adv. Mater.* **2013**, *25* (17), 2474–2480.

(130) Wu, Z.-S.; Sun, Y.; Tan, Y.-Z.; Yang, S.; Feng, X.; Müllen, K. Three-Dimensional Graphene-Based Macro- and Mesoporous Frameworks for High-Performance Electrochemical Capacitive Energy Storage. *J. Am. Chem. Soc.* **2012**, *134* (48), 19532–19535.

(131) Ismanto, A. E.; Wang, S.; Soetaredjo, F. E.; Ismadji, S. Preparation of Capacitor's Electrode from Cassava Peel Waste. *Bioresour. Technol.* **2010**, *101* (10), 3534–3540.

(132) Cheng, P.; Gao, S.; Zang, P.; Yang, X.; Bai, Y.; Xu, H.; Liu, Z.; Lei, Z. Hierarchically Porous Carbon by Activation of Shiitake Mushroom for Capacitive Energy Storage. *Carbon* **2015**, *93*, 315–324.

(133) Sing, K. S. W. Reporting Physisorption Data for Gas/solid Systems with Special Reference to the Determination of Surface Area and Porosity (Recommendations 1984). *Pure Appl. Chem.* **1985**, *57* (4), 603–619.

(134) Zhong, C.; Deng, Y.; Hu, W.; Qiao, J.; Zhang, L.; Zhang, J.; Burke, A.; Simon, P.; Gogotsi, Y.; Naoi, K.; et al. A Review of Electrolyte Materials and Compositions for Electrochemical Supercapacitors. *Chem. Soc. Rev.* **2015**, *44* (21), 7484–7539.

(135) Biswal, M.; Banerjee, A.; Deo, M.; Ogale, S.; Wang, G.; Zhang, L.; Zhang, J.; Frackowiaka, E.; Béguin, F.; Dai, L.; et al. From Dead Leaves to High Energy Density Supercapacitors. *Energy Environ. Sci.* **2013**, *6* (4), 1249.

(136) Lee, J. H.; Park, N.; Kim, B. G.; Jung, D. S.; Im, K.; Hur, J.; Choi, J. W. Restacking-Inhibited 3D Reduced Graphene Oxide for High Performance Supercapacitor Electrodes. *ACS Nano* **2013**, *7* (10), 9366–9374.

(137) Qu, W. H.; Xu, Y. Y.; Lu, A. H.; Zhang, X. Q.; Li, W. C. Converting Biowaste Corncob Residue into High Value Added Porous Carbon for Supercapacitor

Electrodes. *Bioresour. Technol.* **2015**, *189*, 285–291.

(138) Xie, K.; Li, J.; Lai, Y.; Zhang, Z.; Liu, Y.; Zhang, G.; Huang, H. Polyaniline Nanowire Array Encapsulated in Titania Nanotubes as a Superior Electrode for Supercapacitors. *Nanoscale* **2011**, *3* (5), 2202.

(139) Vadiyar, M. M.; Bhise, S. C.; Patil, S. K.; Kolekar, S. S.; Chang, J.-Y.; Ghule, A. V. Comparative Study of Individual and Mixed Aqueous Electrolytes with $ZnFe_2O_4$ Nano-Flakes Thin Film as an Electrode for Supercapacitor Application. *ChemistrySelect* **2016**, *1* (5), 959–966.

(140) Dubal, D. P.; Lee, S. H.; Kim, J. G.; Kim, W. B.; Lokhande, C. D. Porous Polypyrrole Clusters Prepared by Electropolymerization for a High Performance Supercapacitor. *J. Mater. Chem.* **2012**, *22* (7), 3044.

(141) Qian, W.; Sun, F.; Xu, Y.; Qiu, L.; Liu, C.; Wang, S.; Yan, F. Human Hair-Derived Carbon Flakes for Electrochemical Supercapacitors. *Energy Environ. Sci.* **2013**, *7* (1), 379–386.

(142) Bose, S.; Kuila, T.; Mishra, A. K.; Rajasekar, R.; Kim, N. H.; Lee, J. H. Carbon-Based Nanostructured Materials and Their Composites as Supercapacitor Electrodes. *J. Mater. Chem.* **2012**, *22* (3), 767–784.

(143) Salunkhe, R. R.; Lee, Y.-H.; Chang, K.-H.; Li, J.-M.; Simon, P.; Tang, J.; Torad, N. L.; Hu, C.-C.; Yamauchi, Y. Nanoarchitectured Graphene-Based Supercapacitors for Next-Generation Energy-Storage Applications. *Chem. - Eur. J.* **2014**, *20* (43), 13838–13852.

(144) Obreja, V. V. N. On the Performance of Supercapacitors with Electrodes Based on Carbon Nanotubes and Carbon Activated material—A Review. *Phys. E (Amsterdam, Neth.)* **2008**, *40* (7), 2596–2605.

(145) Guo, Y.; Shi, Z.; Chen, M.; Wang, C. Hierarchical Porous Carbon Derived from Sulfonated Pitch for Electrical Double Layer Capacitors. *J. Power Sources* **2014**, *252*, 235–243.

(146) Du, S.; Wang, L.; Fu, X.; Chen, M.; Wang, C. Hierarchical Porous Carbon Microspheres Derived from Porous Starch for Use in High-Rate Electrochemical Double-Layer Capacitors. *Bioresour. Technol.* **2013**; *139*, 106-109.

(147) Wang, R.; Wang, P.; Yan, X.; Lang, J.; Peng, C.; Xue, Q. Promising Porous Carbon Derived from Celtuce Leaves with Outstanding Supercapacitance and CO_2 Capture Performance. *ACS Appl. Mater. Interfaces* **2012**, *4* (11), 5800–5806.

(148) Hegde, G.; Abdul Manaf, S. A.; Kumar, A.; Ali, G. A. M.; Chong, K. F.; Ngaini, Z.; Sharma, K. V. Biowaste Sago Bark Based Catalyst Free Carbon Nanospheres: Waste to Wealth Approach. *ACS Sustainable Chem. Eng.* **2015**, *3* (9), 2247–2253.

(149) Xie, Q.; Bao, R.; Zheng, A.; Zhang, Y.; Wu, S.; Xie, C.; Zhao, P. Sustainable Low-Cost Green Electrodes with High Volumetric Capacitance for Aqueous Symmetric Supercapacitors with High Energy Density. *ACS Sustainable Chem. Eng.* **2016**, *4* (3), 1422–1430.

(150) Zhang, J.; Gong, L.; Sun, K.; Jiang, J.; Zhang, X. Preparation of Activated Carbon from Waste Camellia Oleifera Shell for Supercapacitor Application. *J. Solid State Electrochem.* **2012**, *16* (6), 2179–2186.

(151) Ferrero, G. A.; Fuertes, A. B.; Sevilla, M. From Soybean Residue to Advanced Supercapacitors. *Sci. Rep.* **2015**, *5*, 16618.

(152) Yang, Y.; Ruan, G.; Xiang, C.; Wang, G.; Tour, J. M. Flexible Three-Dimensional Nanoporous Metal-Based Energy Devices. *J. Am. Chem. Soc.* **2014**, *136* (17), 6187–6190.

(153) Cui, H.; Zhu, G.; Liu, X.; Liu, F.; Xie, Y.; Yang, C.; Lin, T.; Gu, H.; Huang, F. Niobium Nitride Nb_4N_5 as a New High-Performance Electrode Material for Supercapacitors. *Adv. Sci.* **2015**, *2* (12), 1500126.

(154) Yu, J.; Lu, W.; Pei, S.; Gong, K.; Wang, L.; Meng, L.; Huang, Y.; Smith, J. P.; Booksh, K. S.; Li, Q.; et al. Omnidirectionally Stretchable High-Performance Supercapacitor Based on Isotropic Buckled Carbon Nanotube Films. *ACS Nano* **2016**, *10* (5), 5204–5211.

(155) Cao, J.; Wang, Y.; Chen, J.; Li, X.; Walsh, F. C.; Ouyang, J.-H.; Jia, D.; Zhou, Y. Three-Dimensional Graphene Oxide/polypyrrole Composite Electrodes Fabricated by One-Step Electrodeposition for High Performance Supercapacitors. *J. Mater. Chem. A* **2015**, *3* (27), 14445–14457.

(156) Liu, N.; Ma, W.; Tao, J.; Zhang, X.; Su, J.; Li, L.; Yang, C.; Gao, Y.; Golberg, D.; Bando, Y. Cable-Type Supercapacitors of Three-Dimensional Cotton Thread Based Multi-Grade Nanostructures for Wearable Energy Storage. *Adv. Mater.* **2013**, *25* (35), 4925–4931.

(157) Le, V. T.; Kim, H.; Ghosh, A.; Kim, J.; Chang, J.; Vu, Q. A.; Pham, D. T.; Lee, J.-H.; Kim, S.-W.; Lee, Y. H. Coaxial Fiber Supercapacitor Using All-Carbon Material Electrodes. *ACS Nano* **2013**, *7* (7), 5940–5947.

(158) Weng, Z.; Su, Y.; Wang, D.-W.; Li, F.; Du, J.; Cheng, H.-M. Graphene-Cellulose Paper Flexible Supercapacitors. *Adv. Energy Mater.* **2011**, *1* (5), 917–922.

(159) Masarapu, C.; Zeng, H. F.; Hung, K. H.; Wei, B. Effect of Temperature on the Capacitance of Carbon Nanotube Supercapacitors. *ACS Nano* **2009**, *3* (8), 2199–2206.

(160) Desroches, M.; Caillol, S.; Lapinte, V.; Auvergne, R.; Boutevin, B. Synthesis of Biobased Polyols by Thiol−Ene Coupling from Vegetable Oils. *Macromolecules* **2011**, *44* (8), 2489–2500.

APPENDIX

APPENDIX

List of Publications

Peer-reviwed journal articles published (or under review) from this thesis work

(1) **Ranaweera, C. K.;** Ionescu, M.; Bilic, N.; Wan, X.; Kahol, P. K.; Gupta, R. K. Biobased Polyols Using Thiol-Ene Chemistry for Rigid Polyurethane Foams with Enhanced Flame-Retardant Properties. *J. Renew. Mater.* **2017**, 1–12

(2) **Ranaweera, C.K**.; Kahol, P. K.; Ghimire, M.; Mishra, S.R; Gupta, R.K. Architecting the carbon derived from orange peel for sustainable and high performing supercapacitor electrodes. *ACS Sustain. Chem. Eng.* **2017**, (Under review)

Other peer-reviwed journal articles published during Master's program

(1) Alkhalaf, S.; **Ranaweera, C. K**.; Kahol, P. K.; Siam, K.; Adhikari, H.; Mishra, S. R.; Perez, F.; Gupta, B. K.; Ramasamy, K.; Gupta, R. K. Electrochemical Energy Storage Performance of Electrospun $CoMn_2O_4$ Nanofibers. *J. Alloys Compd*. **2017**, 692.

(2) Adhikari, H.; Ghimire, M.; **Ranaweera, C. K**.; Bhoyate, S.; Gupta, R. K.; Alam, J.; Mishra, S. R. Synthesis and Electrochemical Performance of Hydrothermally Synthesized $Co_3 O_4$ Nanostructured Particles in Presence of Urea. *J. Alloys Compd*. **2017**, 708, 628–638.

(3) Adhikari, H.; Neupane, D.; **Ranaweera, C. K**.; Candler, J.; Gupta, R. K.; Sapkota, S.; Shen, X.; Mishra, S. R. Template-Free Synthesis of Hierarchical Mixed-Metal Cobaltites: Electrocapacitive and Theoretical Study. *Electrochim. Acta* **2017**, 225, 514–524.

(4) **Ranaweera, C. K**.; Wang, Z.; Alqurashi, E.; Kahol, P. K.; Dvornic, P. R.; Gupta, B. K.; Ramasamy, K.; Mohite, A. D.; Gupta, G.; Gupta, R. K. Highly Stable Hollow Bifunctional Cobalt Sulfides for Flexible Supercapacitors and Hydrogen Evolution. *J. Mater. Chem. A* **2016**, 4 (23), 9014–9018.

(5) Zequine, C.; **Ranaweera, C. K**.; Wang, Z.; Singh, S.; Tripathi, P.; Srivastava, O. N.; Gupta, B. K.; Ramasamy, K.; Kahol, P. K.; Dvornic, P. R.; et al. High per Formance and Flexible Supercapacitors Based on Carbonized Bamboo Fibers for Wide Temperature Applications. *Sci. Rep*. **2016**, 6.

(6) Adhikari, H.; **Ranaweera, C**.; Gupta, R.; Mishra, S. R. Facile Hydrothermal Synthesis of Molybdenum Disulfide (MoS2) as Advanced Electrodes for Super Capacitors Applications. *MRS Adv*. **2016**, No. August, 1–9.

List of Conferance Presentaions

Posters and oral presentations in conferance based on this thesis work

1) **Ranaweera. C.K.**, Ionescu. M., Bilic. N., Wan X., Pawan K., Gupta. R.K, "Bio-based Polyols via Thiol-Ene "Click" Chemistry for Fire Resistance Rigid Polyurethane Foams", 63rd ACS Pentasectional Regional Meeting, Lawton, Oklahoma, March 25, 2017

2) **Ranaweera. C.K.**, Ionescu. M., Bilic. N., Wan X., Pawan K., Gupta. R.K., "From bio-waste to flame retardant polyurethanes for industrial applications", Capitol Graduate Research Summit, Topeka, Kansas, March 10, 2017

3) **Ranaweera. C.K.**, Ionescu. M., Bilic. N., Wan X., Gupta. R.K., "Bio-based Polyols using Thiol-Ene Chemistry for Rigid Polyurethane Foams with Enhanced Flame

Retardant Properties", Thermoplastic Resin Formulators Association 2017 Annual Meeting, Raleigh, North Carolina, March 5-7, 2017

4) **Ranaweera. C.K.**, Wang. Z., Bilic. N., Ionescu. M., Gupta. R., "Synthesis of Bio-Polyols from Bio-waste using Thiol-Ene "Click" Chemistry for Flame Retardant Polyurethane Foams", 15th Annual K-INBRE Symposium, Manhattan, Kansas, January 14-15, 2017

5) **Ranaweera. C.**, Wang. Z., Kahol. P., Gupta, R. K., "Sustainable, low-cost and flexible supercapacitor device; bio-waste to high performance energy storage", Materials Research Society Fall Meeting and Exhibit, Boston, Massachusetts, November 27-December 2, 2016

6) **Ranaweera. C.**, Wang. Z., Bilic. N., Ionescu. M., Gupta. R., "Renewable Polyols using Thiol-Ene "Click" Chemistry for Flame Retardant Polyurethane Rigid Foams", ACS- 51st Midwest Regional Meeting, Manhattan, Kansas, October 26-28, 2016

7) **Ranaweera. C.**, Gupta. R. K., "Bio-waste derived high performance and flexible energy storage devices", PSU Student Research Colloquium, Pittsburg, Kansas, April 7, 2016

8) **Ranaweera. C.**, Wang. Z., Gupta. R. K., "Orange Peel, A Bio-Waste for High Performance Energy Storage Applications", Energy Materials Nanotechnology Meeting on Batteries, Orlando, Florida, February 21-25, 2016 (Invited)

9) **Ranaweera. C.**, Wang. Z., Kahol. P. K., Dvornic. P. R, Gupta, R. K., "Orange Peels for Supercapacitor Applications", 14th Annual K-INBRE Symposium, Overland Park, Kansas, January 16-17, 2016

Other posters and oral presentations in conference during the Master's program

1) **Ranaweera. C.**, Sanket. S., Zhang. C., Kahol. P.K., Gupta. R. K., "Polymer derived carbon nanofiber embedded cobalt oxide for efficient supercapacitors with improve performance at high temperatures", PSU Student Research Colloquium, Pittsburg, Kansas, April 6, 2017
2) **Ranaweera. C.**, Wang. Z., Gupta. R. K., "Promising activated carbons derived from bio-waste for high performance energy storage devices", 62nd ACS Pentasectional Regional Meeting, Bartlesville, Oklahoma, April 8, 2016

Awards and Recognition for Thesis Work

Awards

1) 7th Excellence in Thermoset Polymer Research Award, Thermoset Resin Formulators Association, 2017
2) Excellence in Research Award, Graduate School, Pittsburg State University, 2016

Media Coverage

1) Covered in local news, "PSU student researches newer, safer materials made from orange peel waste", 03/17/2017
2) Article on PSU website, "Student recognized for environmentally friendly research", 03/13/2017
3) Covered for the news in KSN TV, "PSU student's innovation helps create a away to reduce fossil fuel use", 03/14/2017
4) Joplin Regional Bussiness Journal, "Green Maker-PSU chemistry faculty professor breaking ground in creating affordable, sustainable energy", 07/04/2016